SANDIA REPORT

SAND2007-5876

Unlimited Release

Printed September 2007

Conjugate Heat Transfer Analysis using the Calore and Fuego Codes

Nicholas D. Francis, Jr.

Prepared by Sandia National Laboratories

Albuquerque, New Mexico 87185 and Livermore, California 94550

Sandia is a multiprogram laboratory operated by Sandia Corporation,

a Lockheed Martin Company, for the United States Department of Energy's National Nuclear Security Administration under Contract DE-AC04-94AL85000.

Issued by Sandia National Laboratories, operated for the United States Department of Energy by Sandia Corporation.

Available to DOE and DOE contractors from
U.S. Department of Energy
Office of Scientific and Technical Information
P.O. Box 62
Oak Ridge, TN 37831

Telephone: (865)576-8401
Facsimile: (865)576-5728
E-Mail: reports@adonis.osti.gov
Online ordering: http://www.osti.gov/bridge

Available to the public from
U.S. Department of Commerce
National Technical Information Service
5285 Port Royal Rd
Springfield, VA 22161

Telephone: (800)553-6847
Facsimile: (703)605-6900
E-Mail: orders@ntis.fedworld.gov
Online order: http://www.ntis.gov/help/ordermethods.asp?loc=7-4-0#online

SAND2007-5876
Unlimited Release
Printed September 2007

Conjugate Heat Transfer Analysis using the Calore and Fuego Codes

Nicholas D. Francis, Jr.
Thermal and Reactive Processes Department 1516

Sandia National Laboratories
P. O. Box 5800
Albuquerque, NM 87185

Abstract

Full coupling of the Calore and Fuego codes has been exercised in this report. This is done to allow solution of general conjugate heat transfer applications that require more than a fluid flow analysis with a very simple conduction region (solved using Fuego alone) or more than a complex conduction/radiation analysis using a simple Newton's law of cooling boundary condition (solved using Calore alone). Code coupling allows for solution of both complex fluid and solid regions, with or without thermal radiation, either participating or non-participating.

A coupled physics model is developed to compare to data taken from a horizontal concentric cylinder arrangement using the Penlight heating apparatus located at the thermal test complex (TTC) at Sandia National Laboratories. The experimental set-up requires use of a conjugate heat transfer analysis including conduction, non-participating thermal radiation, and internal natural convection. The fluids domain in the model is complex and can be characterized by stagnant fluid regions, laminar circulation, a transition regime, and low-level turbulent regions, all in the same domain. Subsequently, the fluids region requires a refined mesh near the wall so that numerical resolution is achieved. Near the wall, buoyancy exhibits its strongest influence on turbulence (i.e., where turbulence conditions exist). Because low-Reynolds number effects are important in anisotropic natural convective flows of this type, the $\overline{v^2}$-f turbulence model in Fuego is selected and compared to results of laminar flow only.

Coupled code predictions are compared to temperature measurements made both in the solid regions and a fluid region. Turbulent and laminar flow predictions are nearly identical for both regions. Predicted temperatures in the solid regions compare well to data. The largest discrepancies occur at the bottom of the annulus. Predicted temperatures in the fluid region, for the most part, compare well to data. As before, the largest discrepancies occur at the bottom of the annulus where the flow transitions to or is a low-level turbulent flow.

Acknowledgements

Review comments from Dean Dobranich, staff member of the Thermal and Reactive Processes Department, Stefan P. Domino, staff member of the Thermal/Fluids Computational Engineering Department, and, E. S. Hertel, manager of the Thermal and Reactive Processes Department, are greatly appreciated. Their insightful comments have made this a much better document.

Contents

Figures

Tables

Nomenclature

V&V	Verification and Validation
ASC	Advanced Simulation and Computing
TTC	Thermal Test Complex
CFD	Computational Fluid Dynamics
TC#	Thermocouple #
TG#	Gas Temperature #
Ra_L	Rayleigh number based on gap width
URF	Under-Relaxation Factor
GMRES	Generalized Minimum Residual
DD-ILUT	Domain Decomposition, ILUT sparse factorization
CG	Conjugate Gradient
MUSCL	Monotonic Upwind Schemes for Conservation Laws
Tbird	*Thunderbird* Linux Cluster
CFL	Courant-Friedrichs-Lewy number
BICGSTAB	Biconjugate Gradient with Stabilization
TFNS	Temporally Filtered Navier-Stokes

Introduction

Thermal environment verification and validation (V&V) activities typically involve very detailed formulations for conduction and enclosure thermal radiation heat transfer. These activities are performed with a heat transfer code. The impact of fluid-flow-driven heat transfer has typically been approximated in the stand-alone use of the heat transfer code. External convection heat transfer (usually applied at a model boundary via Newton's law of cooling) is included in a V&V analysis by assuming a correlation based heat transfer coefficient obtained from traditional geometries and steady-state fluid conditions (i.e., a constant temperature infinite vertical wall). In many instances this is a reasonable simplification for external convection heat transfer from a standard modeled geometry. Internal convection heat transfer is even more complicated and requires more extensive assumptions to simplify the application. In some instances, a standard correlation coefficient can be applied to an internal fluids region with the use of a bulk fluid energy balance. The bulk fluid element represents the solution of an integral form of the energy conservation equation to determine the mean temperature of the fluid within the enclosed volume. This approach may in fact be adequate for applications in which the fluid temperature and flow conditions are essentially uniform; however, it is not likely to be applicable to the case in which flow conditions and fluid temperature change with location in the enclosure. This more general case requires further refinement of the fluids region, necessitating the introduction of a fluid flow code along with the heat transfer code.

The ASC program is emphasizing coupled physics that accurately reflects the actual physical environment. To support the move from single to coupled physics, there exists a need to validate the coupling approach and key physical processes. This V&V project develops a coupled physics model and compares coupled model predictions directly to experimentally measured data associated with heating in an internal enclosure.

This particular project focuses on coupling between the Calore and Fuego codes and the convective heat transfer processes associated with the more general problem of conjugate heat transfer. It stresses the features of fluid and heat flow in complex regions including both fluids and solids. Specifically, it highlights the use of conductive heat transfer in a solid region that is coupled to the convective heat transfer in a neighboring fluid region, non-participating enclosure thermal radiation across the fluid gap, and finally, conduction through other adjacent solid materials. Experimental temperature measurements are obtained in both the solid and fluid regions at a number of different locations. Model predictions of temperature are compared at each of the locations. This initial approach to model validation is one that lends

confidence in complex coupling between a code with the capabilities of computational fluid dynamics (Fuego[1]) to a computational heat transfer code including enclosure radiation (Calore[2]).

Modeled Geometry

This section of the report describes both the experimental apparatus located at the thermal test complex (TTC) at Sandia National Laboratories and the coupled model development.

Experimental Apparatus

The solids regions are relatively straightforward in both geometry and material composition. The applied materials are typical metals and insulating materials used in experiments performed at the TTC. Detailed, well understood, formulations for conduction and enclosure (surface-to-surface) thermal radiation heat transfer processes are included in these regions. The solids domain in this analysis includes the metallic outer and inner cylinders and the insulation fill materials both inside the inner cylinder and enclosing the sides of the air space annulus between cylinders, refer to Figure 1.

The fluid region is straightforward in geometry and material composition (air), but the natural convective flow processes occurring within are somewhat more complex. It is assumed in this analysis that the air in the fluids region is a non-participating medium. This assumption should be reasonable as this test does not include a combustion process. It is noted that Fuego is being used in this V&V project for computational fluid dynamics (CFD) only. Temperature differences associated with the enclosure surfaces drive convective fluid motion within the enclosure. The fluid domain in this analysis is defined to be the air space enclosed within the annulus formed by the horizontal concentric cylinders and the insulation end-caps shown in Figure 1. The outer cylinder (shroud) is at a higher temperature than the inner cylinder (with test section). The primary test section portion of the inner cylinder is not actually visible in Figure 1 because it is obscured by the end-cap insulation, shroud, and lamp array. Figure 2 isolates the test section and the temperature sensing instrumentation placed on the *inside* of the inner cylinder adjacent to the insulation fill material.

---

[1] SIERRA/Fuego Users Manual – 2.5, SAND2006-6084P, Sandia National Laboratories, June 4, 2007.

[2] Calore; A Computational Heat Transfer Program. User Reference Manual version 4.4, Sandia National Laboratories, October 24, 2006.

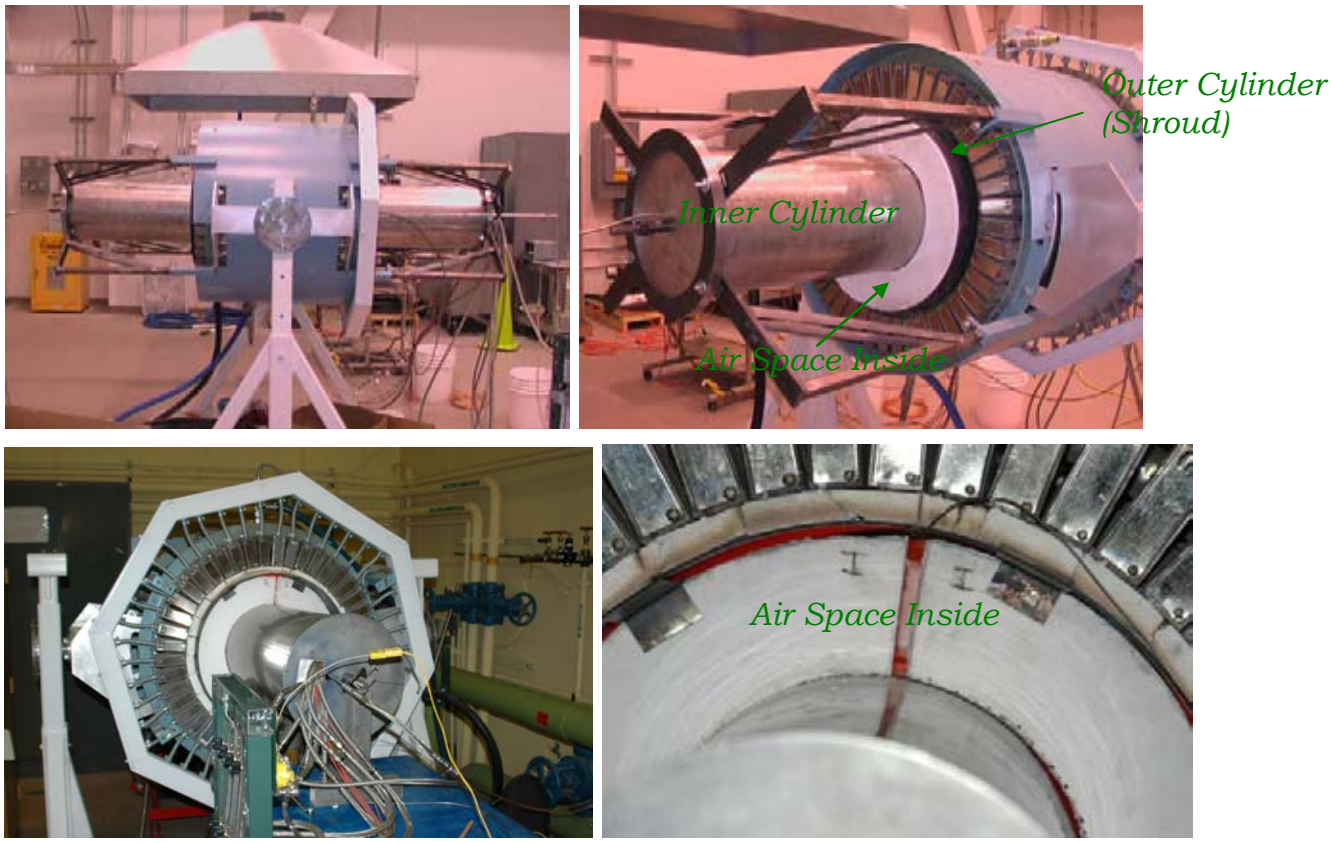

Figure 1. Penlight Test Apparatus for Horizontal Concentric Cylinders.[3]

The stainless steel test section shown in Figure 2 is the part of the inner cylinder centered within the shroud. The test section inner cylinder is where nearly all of the temperature recording devices are located. There are 36 thermocouples located in the solid region test section. There are 4 thermocouples located in the fluid region slightly above the test section cylinder. The solid region thermocouples are placed inside the test section at angular increments of 45° around the circumference of the test section. The gas temperature measurements are located at angular locations 0°, 90°, 180°, and 270°. The angular locations are shown in Figure 3. The experimental data taken on **March 22, 2006,** are compared to coupled model predictions.

[3] Allen Ricks, Thomas Blanchat, and Dann Jernigan, "Validation Experiments to Determine Radiation Partitioning of Heat Flux to an Object in a Fully Turbulent Fire," SAND2006-3494, June 2006.

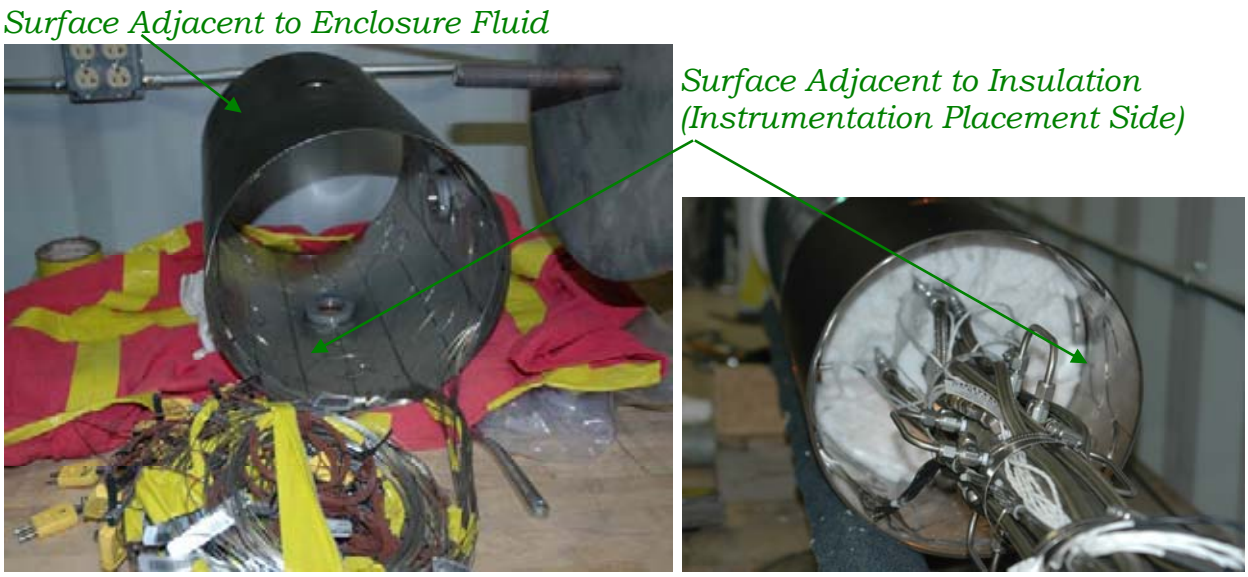

Figure 2. Interior Test Section with Instrumentation and Insulation Fill (See Reference 3).

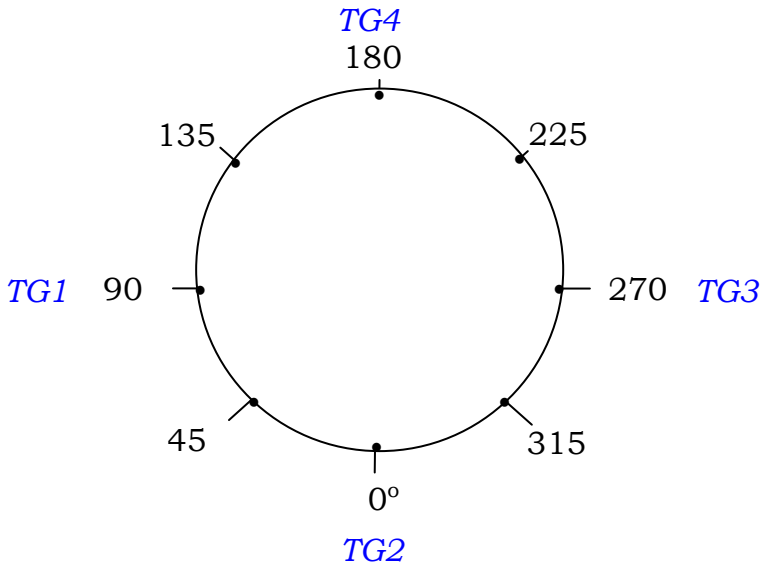

Figure 3. Angular Locations Around the Experimental Test Section for the Test Dated March 22, 2006.

Thermocouple identification numbers are illustrated in Figure 4. So, for example, thermocouples (TCs) 13, 14, 15, and 16 are located at the bottom of the test section cylinder at an angular location of 0°. Note also that TG2, which measures gas temperature, is located at this angular location as well.

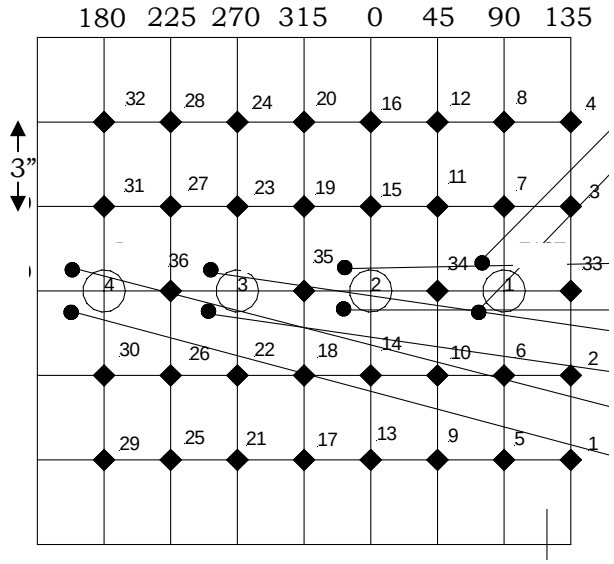

Figure 4. Thermocouple Identifications Associated with Figure 3.

The outer cylinder (shroud) is heated by the surrounding lamp array shown in Figure 1. Twenty eight thermocouples are placed on the shroud to measure its temperature. Thermocouples are located at 90° increments around the circumference of the shroud with seven along the length of the cylinder at each angular location. The intent of the inconel shroud is to essentially provide a uniform temperature heat source for the test section. Implementation of the shroud will be discussed further in the model development section.

Model Development

The Calore region (solids) and Fuego region (fluid) are shown in Figure 5. The Fuego region is shown removed from the interior of the Calore region for illustration purposes. Like Figure 1, the primary test section is obscured by the shroud and insulation end-cap.

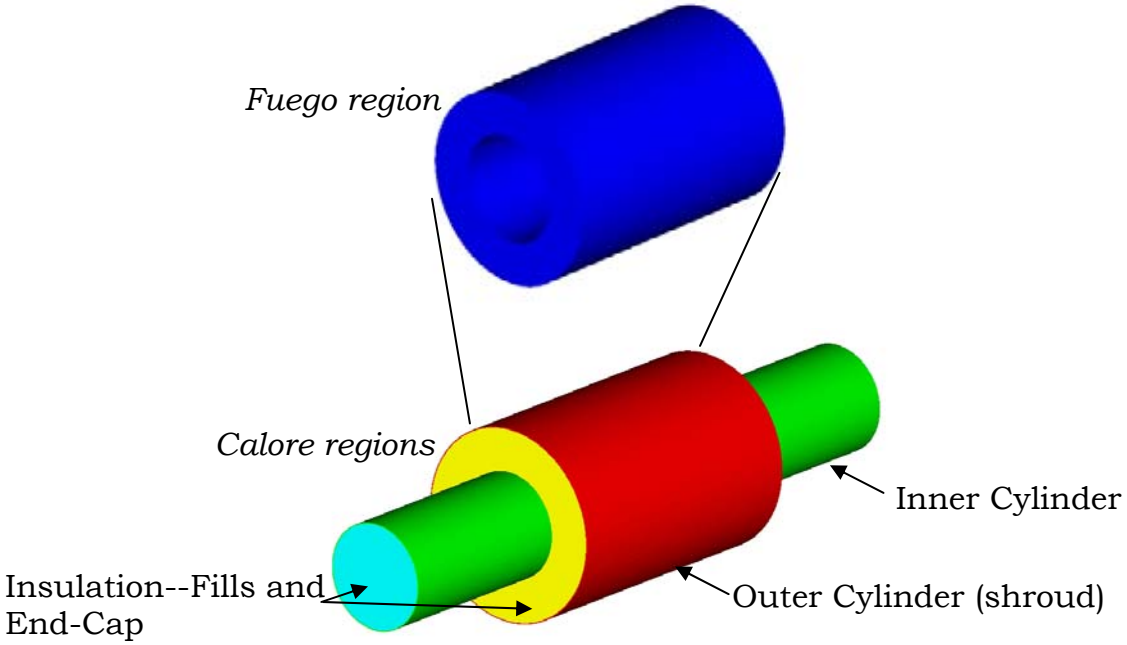

Figure 5. Coupled Model Geometry with Fuego Region Shown Removed from the Calore Region.

The computational mesh associated with the coupled model shown in Figure 5 is shown below in Figure 6.

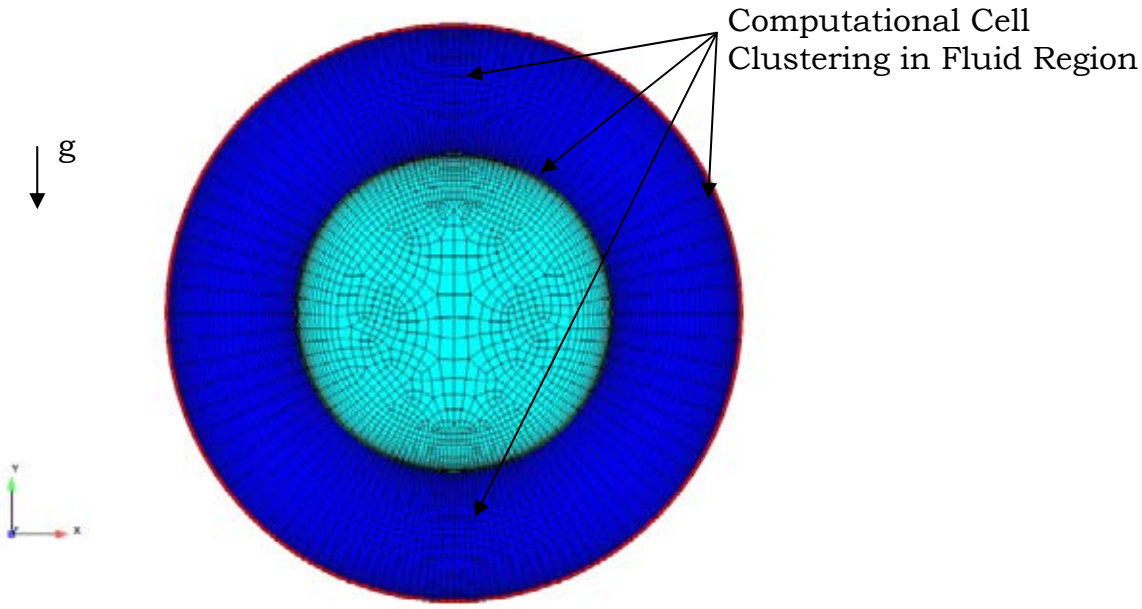

Figure 6. Mesh with Fuego Region Shown in Place.

Figure 6 illustrates computational cell clustering both at the walls (to capture boundary layer effects) and at the top and bottom of the annulus, where the fluid turns. It is further noted that both Calore and Fuego regions are meshed using hexahedral elements. (This element type is typically preferred for fluids meshes; this type is also chosen for the solids mesh, strictly for convenience associated with the information transfer between code regions.) The working mesh has 612,000 total elements; 259,200 elements in the fluid region and 352,800 elements in the solids region. A mesh independence study will be discussed for the laminar flow case described in an upcoming section.

The coupled model boundary conditions include a constant temperature boundary at the shroud, both Newton's law of cooling (using standard correlation equations for external heat transfer) and radiative transport to the environment from the solid regions that do not participate in the enclosure, enclosure radiation across the fluid region, and conjugate heat transfer between the fluid and solid regions associated with the enclosure.

An averaged shroud temperature is shown with all shroud thermocouple measurements in Figure 7. Use of an average shroud temperature greatly simplifies the temperature specification of the outer cylinder (i.e., it makes it a uniform temperature boundary condition). The shroud boundary condition, shown in red in Figure 5 and Figure 6, assumes a (spatially) uniform average temperature associated with the thermocouples with the largest area coverage on the shroud (solid lines shown in the figure). The edge-most thermocouples (dashed lines shown in the figure) have been neglected in the calculation of a straight uniform average shroud temperature because their area coverage is small.

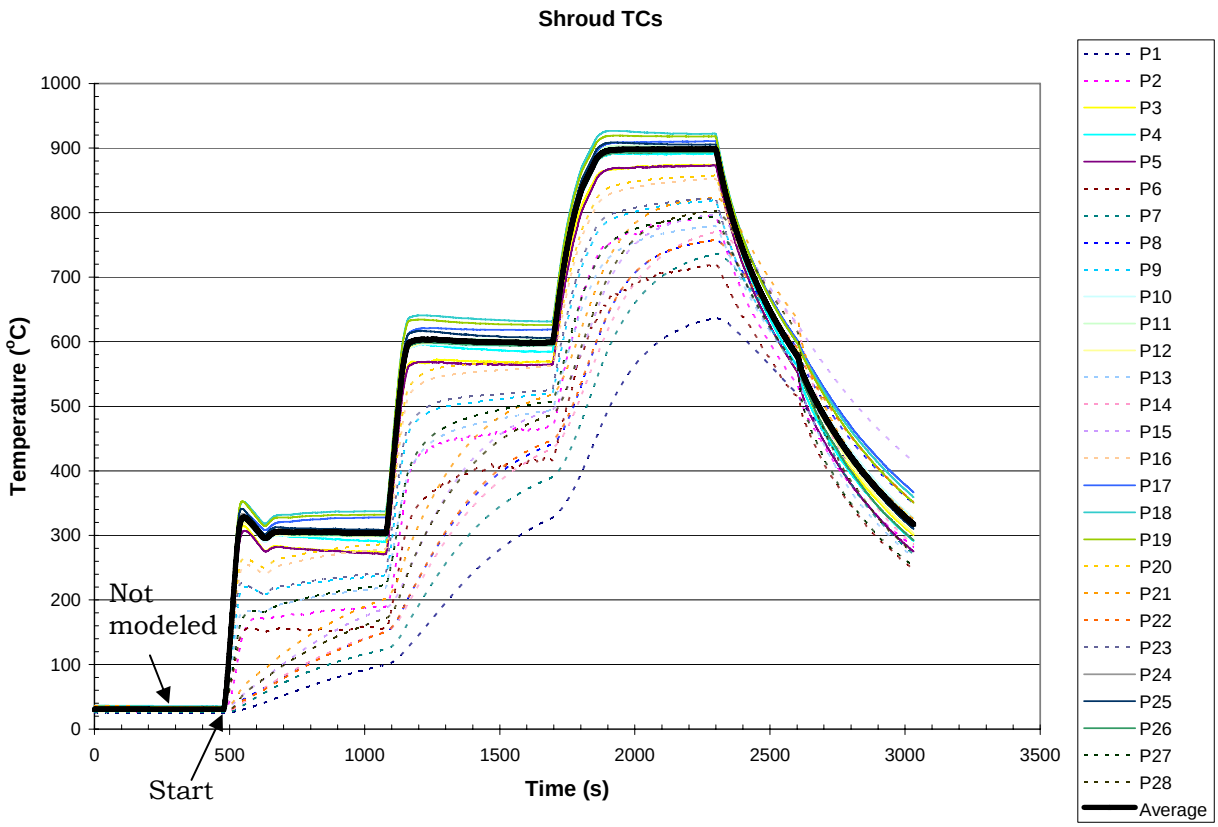

Figure 7. Shroud Measured Temperatures with Average used in the Coupled Model.

An area-weighted average temperature may have been more appropriate than the non-weighted (algebraic) average used in this analysis; however, it was decided that the cooler measured temperatures at the edges of the shroud represented little of the overall shroud surface area. Subsequently, an area-weighted average and a straight average neglecting the cooler edge thermocouples are similar. Use of a more realistic non-uniform (spatial) temperature assignment, for the shroud boundary condition, based on each of the measured temperatures shown in Figure 7 was not attempted to date due to a desire to achieve the simplest, yet still representative, temperature boundary condition possible. More will be said on this simplifying assumption later in the results section.

Fluid Flow Characteristics

The test apparatus shown in Figure 1 and the heating schedule shown in Figure 7 results in a thermally driven buoyant flow in the annulus formed between the horizontal concentric inner and outer cylinders. Fluid flow in the

air space is driven by the temperature difference between cylinders. Flow occurs either upward or downward, depending on wall temperature, primarily in the boundary layers adjacent to the cylindrical walls. The flow turns at the top and bottom of the annulus. It is also noted that flow along the length of the annulus occurs near the ends of the annulus as a result of the insulation end-caps. A natural convection flow field like the one established in this analysis is formally characterized by a Rayleigh number based on gap width:

$$Ra_L = \frac{g\beta\Delta T L^3}{\nu\alpha} \tag{1}$$

where the gap-width is defined in terms of the inner and outer radii as, $R_o - R_i$, α is the fluid thermal diffusivity ($k/\rho c_p$), ν is the fluid kinematic viscosity (μ/ρ), and, β is the volumetric thermal expansion coefficient ($1/T$, for ideal gases). Depending on the boundary conditions, various fluid regimes may coexist. At high Rayleigh numbers (typically > ~10^6 for concentric cylinders), it is not at all unusual to have a variety of different fluid characteristics:

- Stagnant regions
- Laminar circulation
- Transition regime
- Low-level or fully turbulent

within the same fluid domain. Table 1 provides representative Rayleigh numbers evaluated using Equation (1) and listed as a function of simulation time from a laminar flow simulation described later in this report. Overall, Rayleigh numbers decrease with time as the air space warms. Expected flow conditions as a function of Rayleigh number have been previously described in detail for horizontal concentric cylinders[4]. Laminar conditions typically occur for Rayleigh numbers below about 10^5. Oscillations in the rising plume begin to appear at Rayleigh numbers of about $2x10^5$. Portions of the flow become more irregular and fluctuations in the plume increase in intensity at Rayleigh numbers above $1.5x10^6$. Above $2x10^7$, portions of the flow are turbulent.

[4] T. H. Kuehn, and R. J. Goldstein, "An Experimental Study of Natural Convection Heat Transfer in Concentric and Eccentric Horizontal Cylindrical Annuli." Journal of Heat Transfer, Transactions of the ASME, 100, 635-640. 1978.

From Table 1 it is evident that fluctuating and/or turbulent flow conditions potentially exist early, roughly within the first 1000 seconds of heating.

Table 1. Representative Rayleigh (Ra_L) Numbers as a Function of Time.

Simulation Time (s)	Representative Rayleigh Number
30	$7x10^6$
250	$3x10^6$
500	$1.4x10^6$
750	$5.3x10^5$
1300	$1.2x10^5$
1800	$4x10^3$

Consequently, it may be sufficient in this analysis to only consider a turbulent flow simulation during the early portion of the heating schedule, say approximately for the first 1000 seconds of heating, after which time the flow is essentially laminar. This may be beneficial in that it helps reduce the computational burden associated with performing turbulent flow simulations. This approach will be investigated in the following analyses. That is, both laminar and turbulent flow simulations will be performed, but the turbulent flow simulations will only be performed during the early portion of heating.

Buoyancy driven flows require laminar and turbulence flow models that account for low-Reynolds number effects in the near-wall (viscosity affected) region adjacent to a solid boundary[5,6]. Large variations and anisotropies in the flow properties in the near-wall region require fine numerical resolution all-the-way to the solid boundary. This meshing requirement is further necessitated by the fact the universal scaling does not exist for natural convection flows like it does for forced convection flows (e.g., which allows for the application of

[5] K. Hanjalic', "One-Point Closure Models for Buoyancy-Driven Turbulent Flows," Annual Review of Fluid Mechanics, 34, pp. 321-347, 2002.

[6] Nicholas D. Francis, Jr., "Characterization of Fuego for Laminar and Turbulent Natural Convection Heat Transfer, SAND2005-5085, August 2005.

standard wall functions through the viscosity affected region). Therefore, a fine mesh is required near the solid-fluid interfaces (refer to Figure 6) thus driving up model element counts. Reference 6 has explored a variety of different flow models for internal buoyancy driven flows, including the anisotropies associated with low-Reynolds number near-wall behavior. Based on those results, the $\overline{v^2}$-f turbulence model in Fuego is selected for this analysis and compared to the results of laminar flow only. This turbulence model is a four-equation model that represents a compromise between a single-point eddy-viscosity model (i.e., standard k-ε two-equation turbulence model) and a computationally intensive full second-moment closure (i.e., transport equations for Reynolds stresses and turbulent heat flux). It is an appropriate turbulence model for approximating the phenomenon associated with near-wall behavior when integrating all-the-way to the wall.

Laminar Flow Simulations

A number of different laminar flow simulations are performed using the coupled model shown in Figure 5. They include coarse and refined meshes, changes to residual tolerances required for the linear equation solves on continuity and all other scalars (e.g., Y-momentum), different upwind interpolation methods for convection, changes in the number of non-linear iterations, changes in pressure-correction equation under-relaxation factor (URF), and allowing for compressibility effects inside the fluid enclosure. Table 2 lists each of the laminar flow cases including a reference table in which details for a particular simulation may be found. A number of the cases listed in the table are performed in this analysis to improve the speed of the coupled simulations; others are used to assess the influence of the assumptions applied to the working case simulation (#1 in the table). The last column in Table 2 provides a reference to an additional table containing the pertinent details associated with some of the inputs required by the simulations.

All of the laminar flow simulations, except simulations #4 and #5, were executed using 128 processors, simulation #4 used 330 processors and #5 used 40 processors. All simulations were performed on the *Thunderbird* Linux Cluster.

Table 2. Laminar Flow Simulation Descriptions.

#	Legend Entry	Description	Clock (hrs)	Details in
1	Model-Lam, or Model-tight tol, or 6 nonlinear	Working laminar flow simulation	160	Table 3
2	Model-loose tol	Reduced stringency on residual tolerances required for the linear solve on continuity and other scalars	82	Table 4
3	Higher-order conv	Change upwind interpolation for convection	73	Table 4, Table 5
4	Model refined	Refined mesh case	166	Table 4, Table 6
5	Model coarse	Coarse mesh case	31	Table 4, Table 7
6	3 nonlinear	Reduced number of non-linear iterations	57	Table 3, Table 8
7	3 nonlinear, loose tol	Reduced number of non-linear iterations and reduced stringency on residual tolerances	42	Table 4, Table 8
8	3 nonlinear, pressURF	Changes to pressure correction URF, Reduced number of non-linear iterations and reduced stringency on residual tolerances	30	Table 4, Table 9
9	Press	Include compressibility effects in the fluid enclosure	81	Table 4, Table 10

The coupled model details for the working laminar flow simulation (simulation #1 listed in Table 2) are given below in Table 3. This simulation and all others listed in Table 2 uses fourth-order smoothing with timestep scaling as the pressure projection method. The governing conservation equations are solved one-by-one (segregated solver).

Table 3. Details for Laminar Flow Simulation #1.

Model Input	Setting
Fuego continuity solution method	Aztec GMRES
Fuego continuity preconditioning method	DD-ILUT
Residual norm tolerance	10^{-6}
Fuego scalar solution method	Aztec GMRES
Fuego scalar preconditioning method	SYMMETRIC-GAUSS-SEIDEL
Residual norm tolerance	10^{-4}
Calore temperature solution method	Aztec CG
Calore preconditioning method	DD-ICC
Residual norm tolerance	10^{-8}
Upwind method	MUSCL
First order upwind factor	0.5
Fuego non-linear iterations	6
Calore non-linear iterations	5
URF pressure, momentum	0.8, 0.8
Number of hexahedral elements	612,000

Simulation #2 uses model inputs as described in Table 4. Note that the changes from the working case are highlighted in the table in red. This simulation serves solely to increase the speed of the coupled simulations by reducing the stringency on the linear equation solves. It is noted that the solution and preconditioning methods have not been changed; this will be addressed later in this report.

Table 4. Details for Laminar Flow Simulation #2.

Model Input	Setting
Fuego continuity solution method	Aztec GMRES
Fuego continuity preconditioning method	DD-ILUT
Residual norm tolerance	10^{-2}
Fuego scalar solution method	Aztec GMRES
Fuego scalar preconditioning method	SYMMETRIC-GAUSS-SEIDEL
Residual norm tolerance	10^{-2}
Calore temperature solution method	Aztec CG
Calore preconditioning method	DD-ICC
Residual norm tolerance	10^{-6}
Upwind method	MUSCL
First order upwind factor	0.5
Fuego non-linear iterations	6
Calore non-linear iterations	5
URF pressure, momentum	0.8, 0.8
Number of hexahedral elements	612,000

Simulation #3 changes the upwind interpolation method for the convection terms in the fluid flow equations; all other specifications given in Table 4 are also applied here as well. This simulation change is towards a higher order upwinding scheme for convection and is given in Table 5.

Table 5. Change made to Laminar Flow Simulation #3.

Model Input	Setting
First order upwind factor	0.1

Simulation #4 uses a *refined* mesh in both the Calore and Fuego regions. The refined mesh has 1,576,648 total hexahedral elements; 691,200 elements in

the fluid region and 885,448 elements in the solids region. The change made to this simulation is shown in Table 6 with all other solver specifications given in Table 4 applied here as well.

Table 6. Change made to Laminar Flow Simulation #4.

Model Input	Setting
Number of hexahedral elements	1,576,648

Simulation #5 uses a *coarse* mesh in both the Calore and Fuego regions. The coarse mesh has 204,000 total hexahedral elements; 87,360 elements in the fluid region and 116,640 elements in the solids region. The change made to this simulation is shown in Table 7 with all other solver specifications given in Table 4 applied here as well.

Table 7. Change made to Laminar Flow Simulation #5.

Model Input	Setting
Number of hexahedral elements	204,000

Simulation #6 reduces the number of non-linear iterations applied to the fluid flow equations as shown in Table 8, all other specifications given in Table 3 are also applied here as well. Recall that Table 3 provides for the more stringent linear solver tolerance settings. The segregated solution process implemented in Fuego naturally introduces splitting error when the governing equations are solved individually. Taking non-linear iterations is the means by which the non-linearity of the individual equations and the inter-equation couplings are accounted for, thereby reducing the splitting error. Therefore, more non-linear iterations are good from the point of view of reducing the splitting error, but additional iterations result in an increased computational burden. It is reasonable to try to reduce the number of non-linear iterations so as to reduce the computational burden associated with the solution of the governing equations.

Table 8. Change made to Laminar Flow Simulations #6 and #7.

Model Input	Setting
Fuego non-linear iterations	3

Simulation #7 is similar to #6--it also applies Table 8 for the number of Fuego non-linear iterations with the remaining model settings associated with Table 4 instead of Table 3. Recall that Table 4 provides for less stringent linear solver tolerances.

Simulation #8 reduces the pressure-correction under-relaxation factor (URF) and it uses fewer non-linear iterations. The new values are given in Table 9 below with all remaining model settings associated as before with Table 4.

Table 9. Changes made to Laminar Flow Simulation #8.

Model Input	Setting
Fuego non-linear iterations	3
URF pressure, momentum	0.3, 0.8

A final laminar flow simulation (#9) allows for acoustic compressibility effects in the enclosure. Consequently, the additional term Dp/Dt is now added to the right hand side of the energy equation being solved in the fluid region by Fuego. Unfortunately, the ensuing pressure solve experienced unknown difficulties on Tbird (it was *not* diverging, it just randomly aborted at various times during the simulation); therefore, the continuity solution and preconditioning methods changed according to Table 10, with all remaining model settings associated with Table 4. Compressibility is neglected in each of the previous simulations, #1 – 8, described in Table 2. This simulation is used to asses the validity of this simplifying assumption.

Table 10. Change made to Laminar Flow Simulation #9.

Model Input	Setting
Fuego continuity solution method	Trilinos GMRES
Fuego continuity preconditioning method	Multilevel

Before presenting the results of the laminar flow simulations listed in Table 2 and comparing each one to measured temperature data from both the solid and fluid regions, it is necessary to briefly describe the methods used to select an appropriate time step for the coupled model analyses. Again, the balance between accuracy and speed of the computation is considered. It will also be shown how the coupled model compares to a Calore-only computation. The heating schedule applied to the time step study and Calore-only comparison is different (but similar to) that given in Figure 7. This particular study was performed before the experiments were conducted. All other comparisons are performed using the temperature versus time curve from Figure 7.

Time Step Considerations and Comparison to Calore-Only

Three nodes (top, side, and bottom, see inset) are arbitrarily selected for comparison on the surface of the test section directly *adjacent* to the fluid region. The Calore-only result using the hypothetical heating schedule is given in Figure 8. Note that the Calore-only simulation includes conduction and thermal radiation only.

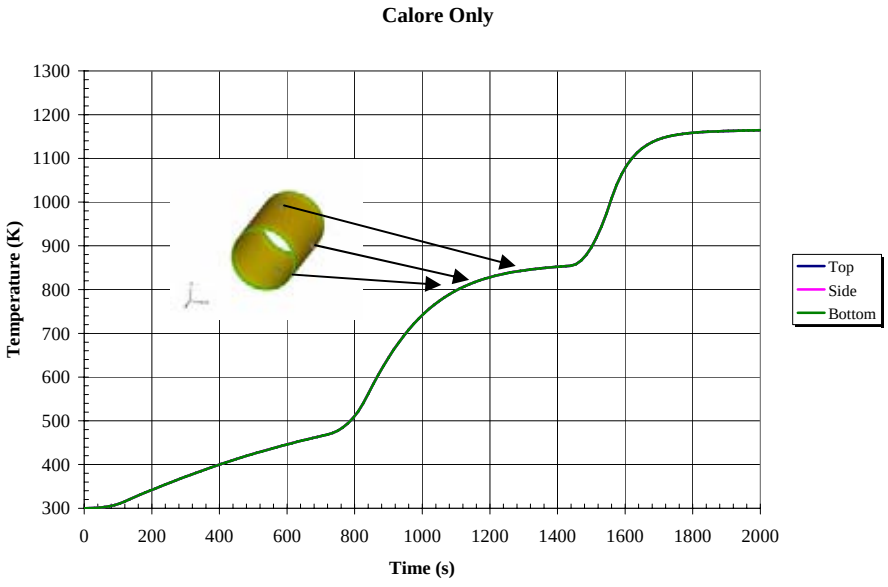

Figure 8. Calore-Only Temperature Results at Top, Side, and Bottom.

As expected, the Calore-only results at each of the three locations, top, side, and bottom, are identical, all three curves shown in Figure 8 overlay each other. The simulation in which laminar flow and conduction and thermal radiation are coupled, top, side, and bottom locations are shown in Figure 9, Figure 10, and Figure 11, respectively.

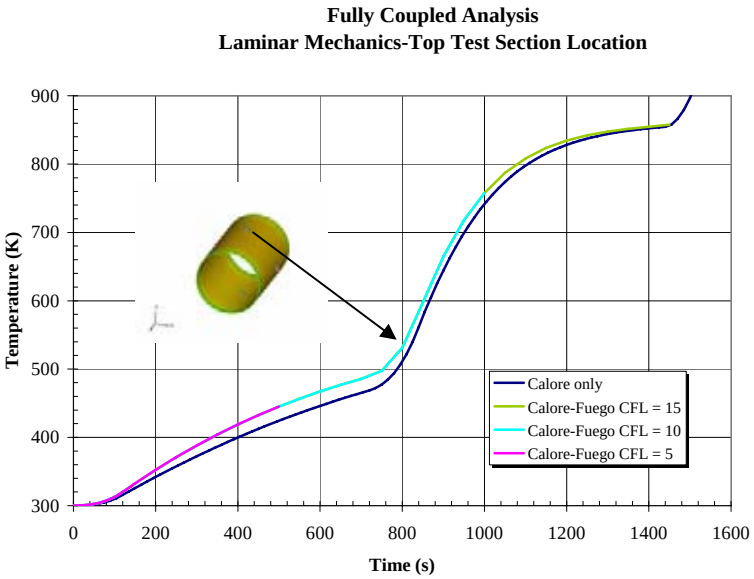

Figure 9. Coupled Model Temperature Result at Top Location.

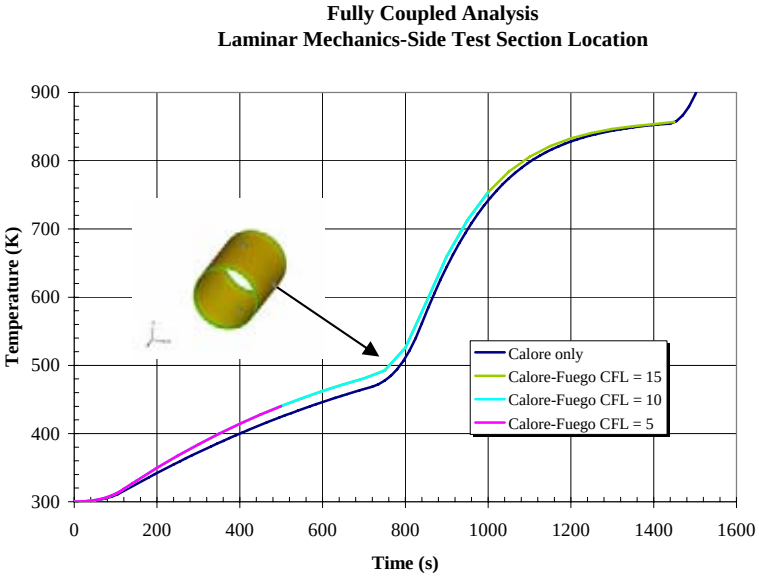

Figure 10. Coupled Model Temperature Result at Side Location.

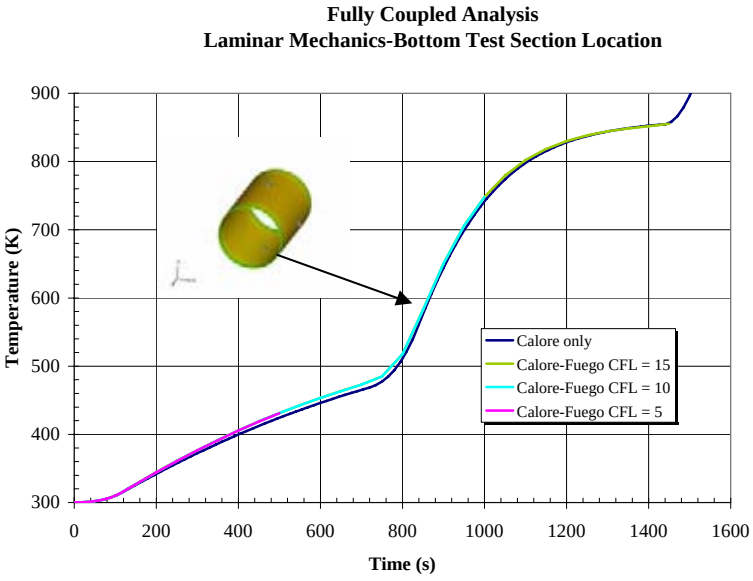

Figure 11. Coupled Model Temperature Result at Bottom Location.

It is noted from Figure 9 - Figure 11 that three different Courant-Friedrichs-Lewy (*CFL)* numbers are used in the coupled model analyses. The *CFL* number is a non-dimensional time step defined in Equation (2) as the following:

$$CFL = \frac{V_{\max}\Delta t}{\Delta x} \tag{2}$$

where $V_{\max}$ is the maximum local fluid velocity, Δx is the cell width, and Δt is the physical time step. It is typically preferred that a *CFL* limit be about 1.0. However, this limit is far too restricting when trying to simulate an appreciable amount of mother-nature time. Therefore, *CFL*s of 5, 10, and 15 are compared in the preceding figures. The overall objective to increase simulated time is achieved as simulated times of 532, 1017, and 1480 seconds are obtained from *CFL*s of 5, 10, and 15, respectively. (For reference, a *CFL* of 1.0 was also considered, but not shown in the figures, with a resulting simulated time of 131 seconds.) Furthermore, it is noted from the figures that the temperature predictions from each of the three cases overlay one another.

Based on these results, a *CFL* limit of 15 is selected for each of the laminar flow simulations described in Table 2. The initial simulation time step is 0.0005

seconds with a time step change factor of 1.2. It is possible that a higher *CFL* may have been selected; however, as the time step gets larger, more non-linear iterations are required. A *CFL* of 15 is selected without having to increase the number of non-linear iterations.

From Figure 9 - Figure 11 it is indicated that the natural convection contribution to the predicted temperature decreases from the top of the test section to the bottom. Furthermore, it is noted that as the inner cylinder heats (later in time), the difference in predicted temperature between the coupled model and the Calore-only simulation decreases, as inferred by Table 1.

Plots of velocity magnitude and gas temperature contours at the center of the fluid region at a time slice of 550 s into heating are illustrated for this hypothetical heating schedule in Figure 12. Unsteady fluid conditions where the flow turns lead to the asymmetrical behavior noted at the top and bottom of the annulus.

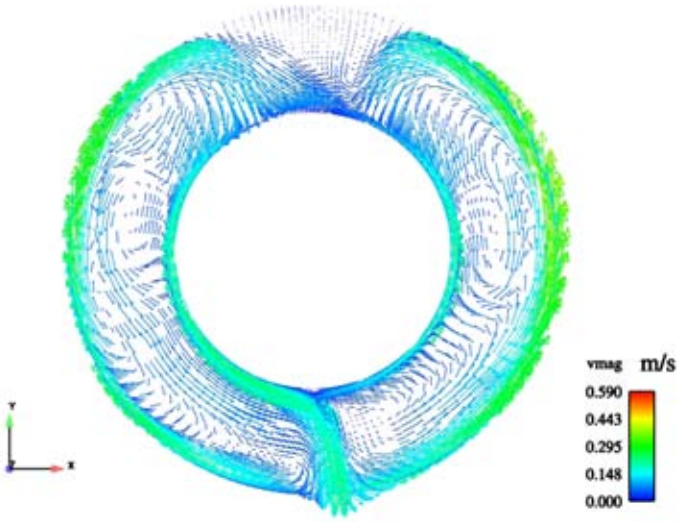

(a) Velocity Magnitude

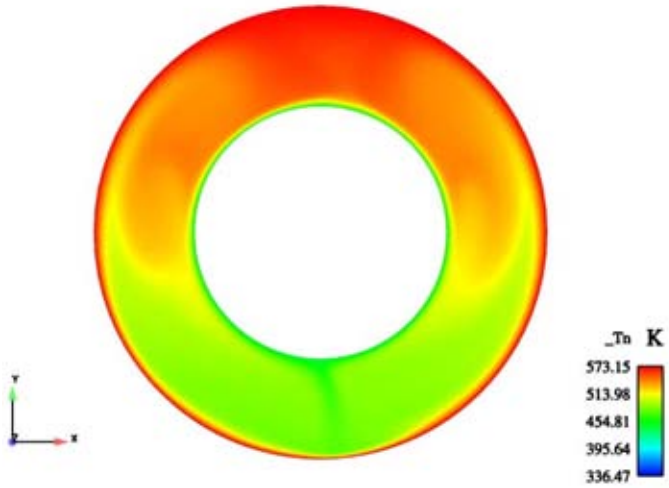

(b) Air Temperature

Figure 12. Fluid Characteristics at 550 s at the Center of the Fluids Region.

Comparison of Laminar Flow Results to Measured Temperature Data

Each of the nine simulations described in Table 2 are plotted in two separate figures for clarity of presentation. Simulations 1 – 5 are given on the first plot, simulations 1, and 6 – 9 are given on the other. The legends in each of the

following figures correspond to the entry given in the second column in Table 2. Thermocouple (TC) locations 1, 5, 9, 13, 17, 21, 25, 29, 33, 34, 35, and 36 are illustrated from the solids region, and, gas temperature (TG) locations 1, 2, 3, and 4 are illustrated from the fluid region. TCs 1, …, 29 represent edge like locations on the test section while TC locations 33 – 36 represent center test section locations at the center of the annulus. TG locations are near the center of the test section near the center of the annulus. The coupled model results shown in this section are all based on the approximation of the experimental heating schedule as shown in Figure 7. Figure 13 through Figure 16 illustrate the coupled model temperature predictions, with comparison to measured data, in the solids region at these TC locations. Figure 17 and Figure 18 illustrate the coupled model temperature predictions, with comparison to measured data, in the fluid region at these TG locations. It is noted that the gas temperature measurements are corrected for thermal radiation effects as described in Reference 3 in section 2.1.2.2 of that document. Subsequently, the comparison made at the four TG locations in this report is for a fluid temperature measurement without a thermal radiation contribution.

In each of the following figures presented for the laminar flow cases, it is noted that all of the predicted temperature curves essentially *overlay* one another. This is indeed the desired result as the coupled flow simulations developed for this analysis and listed in Table 2 are performed to either increase the efficiency of a computation (by reducing the wall clock time) or to assess the appropriateness of an assumption applied to the model.

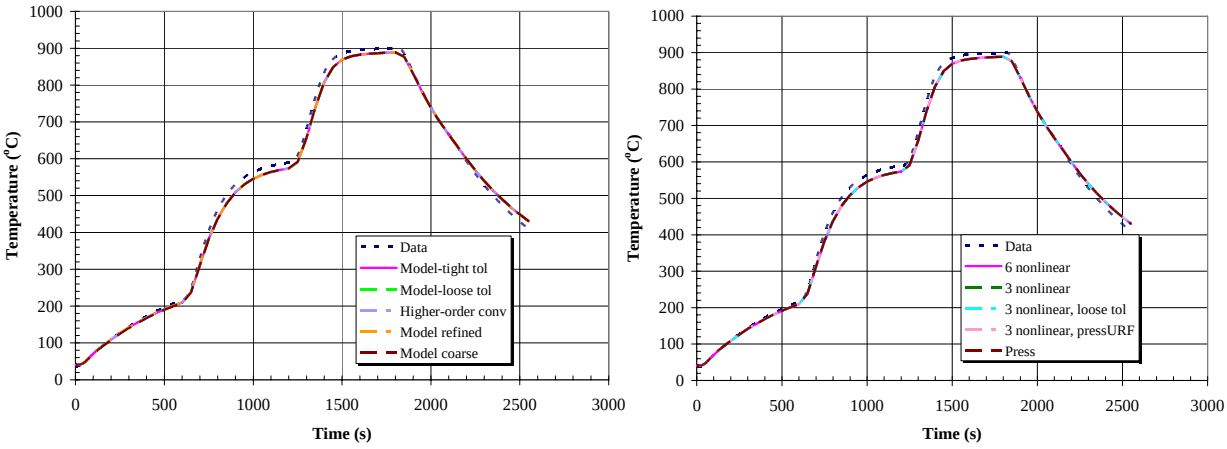

(a) TC1

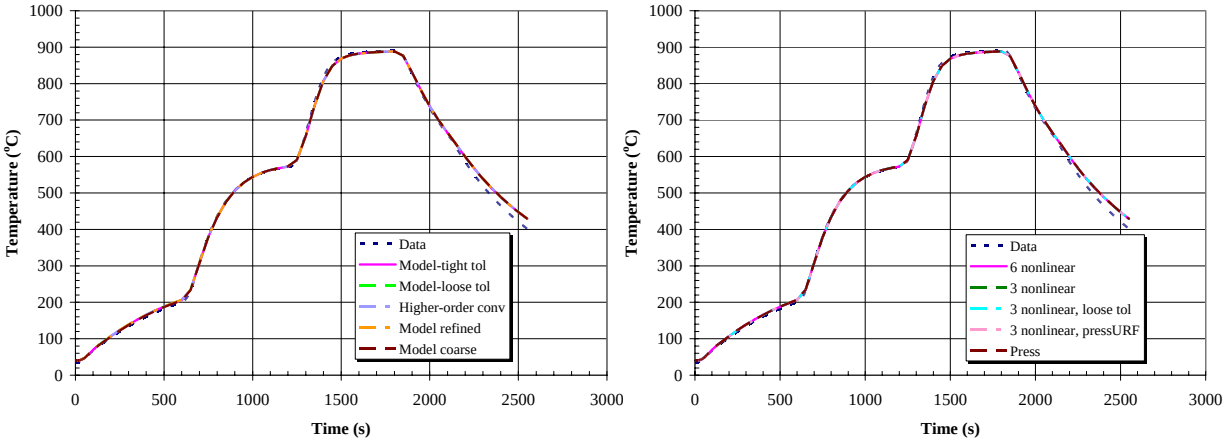

(b) TC5

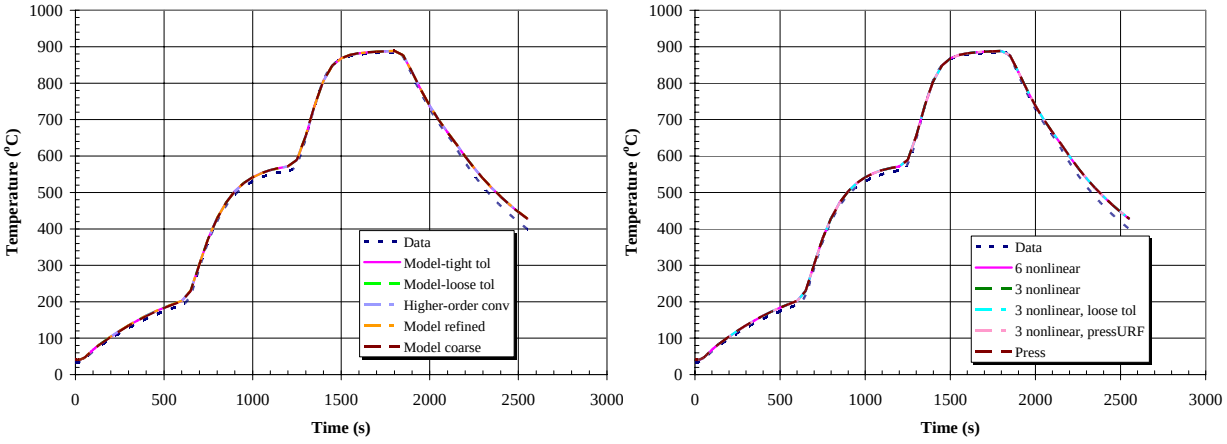

(c) TC9

Figure 13. Laminar Flow Results Comparison to Measure Data, (a) TC1, (b) TC5, and (c) TC9.

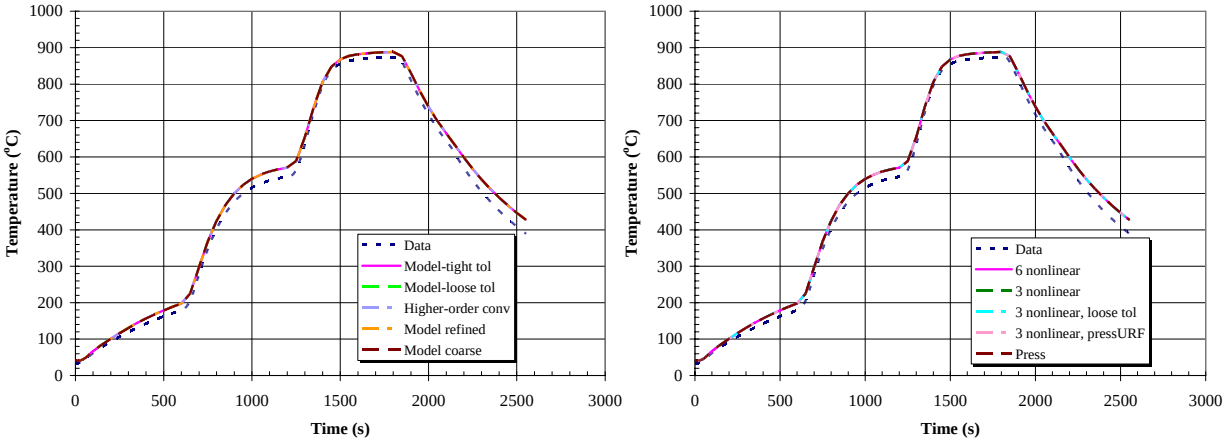

(d) TC13

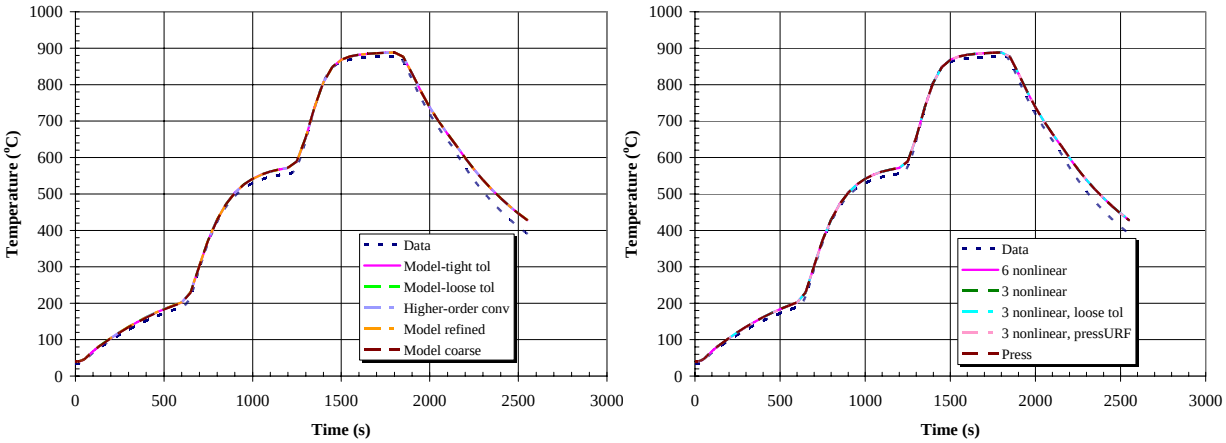

(e) TC17

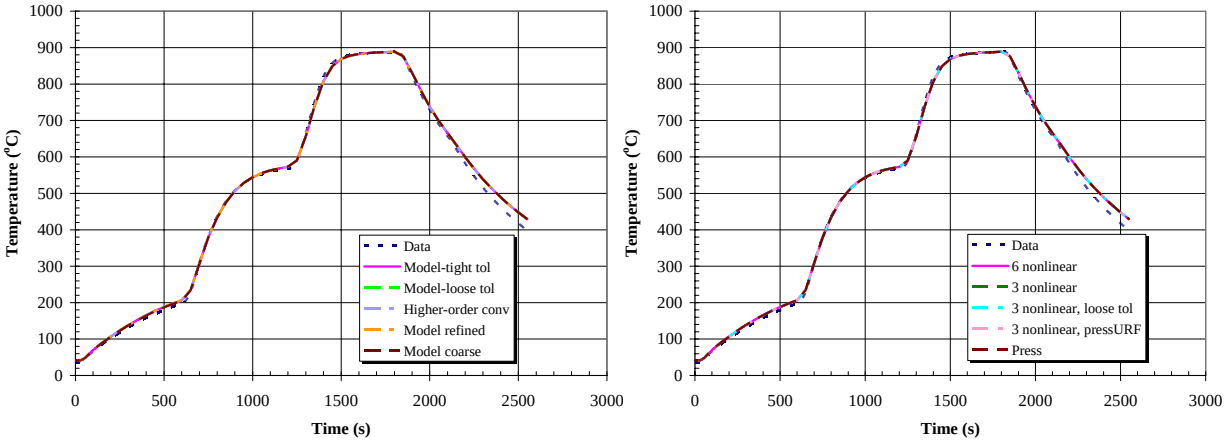

(f) TC21

Figure 14. Laminar Flow Results Comparison to Measure Data, (d) TC13, (e) TC17, and (f) TC21.

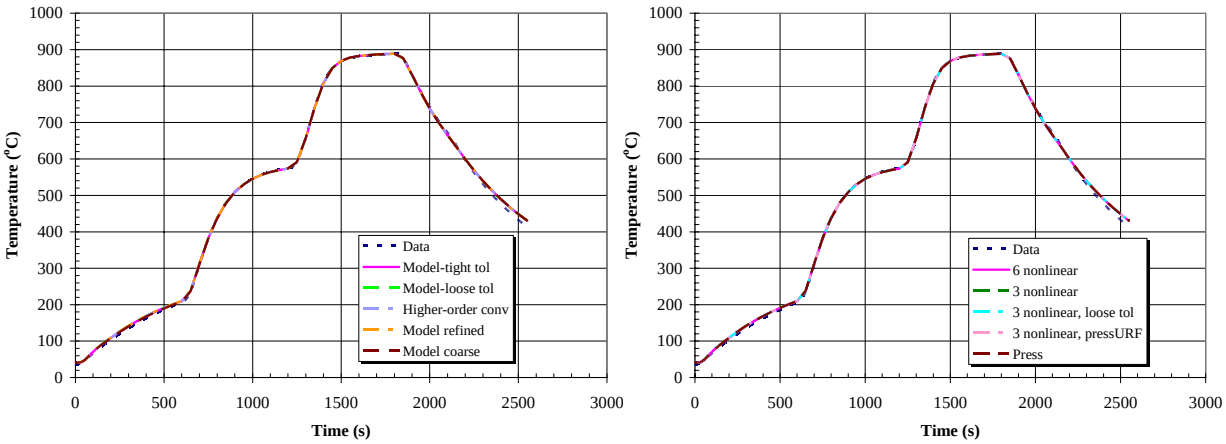

(g) TC25

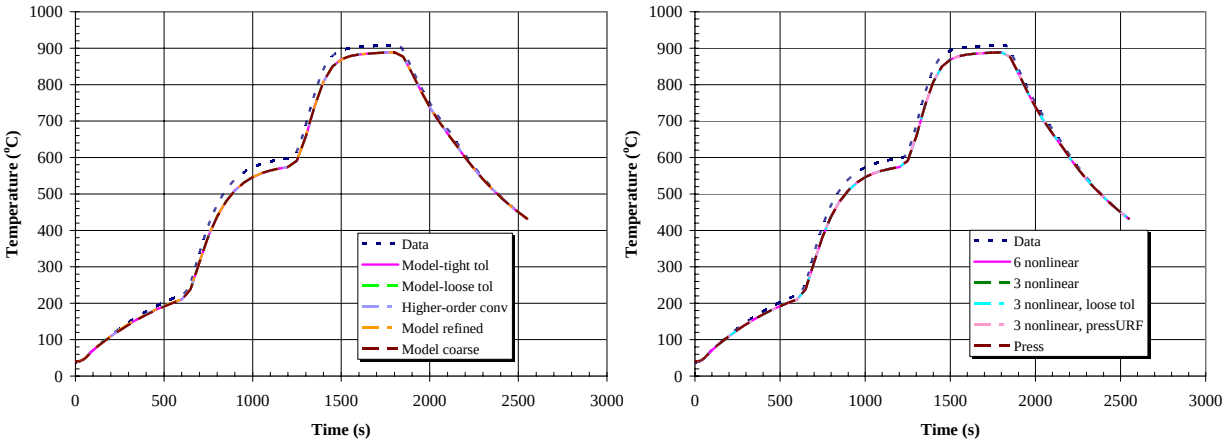

(h) TC29

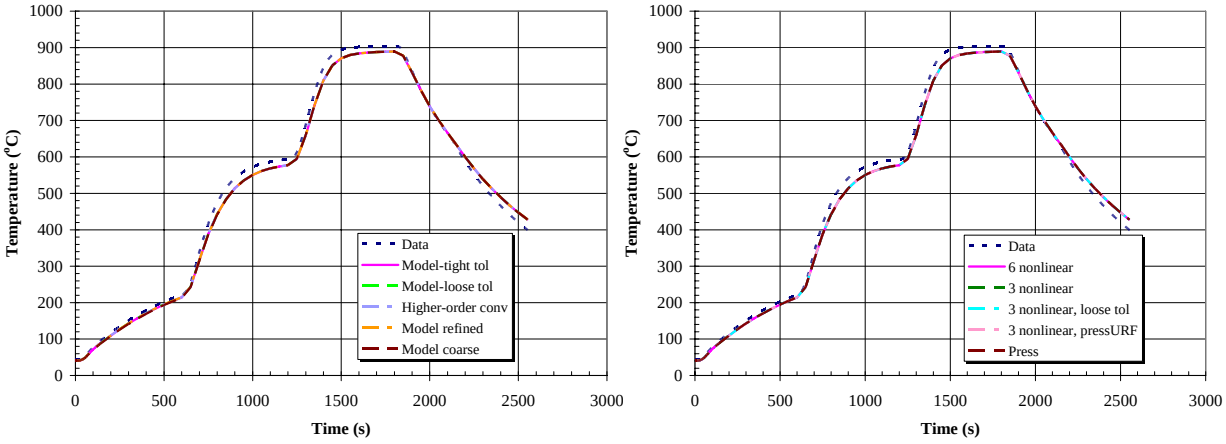

(i) TC33

Figure 15. Laminar Flow Results Comparison to Measure Data, (g) TC25, (h) TC29, and (i) TC33.

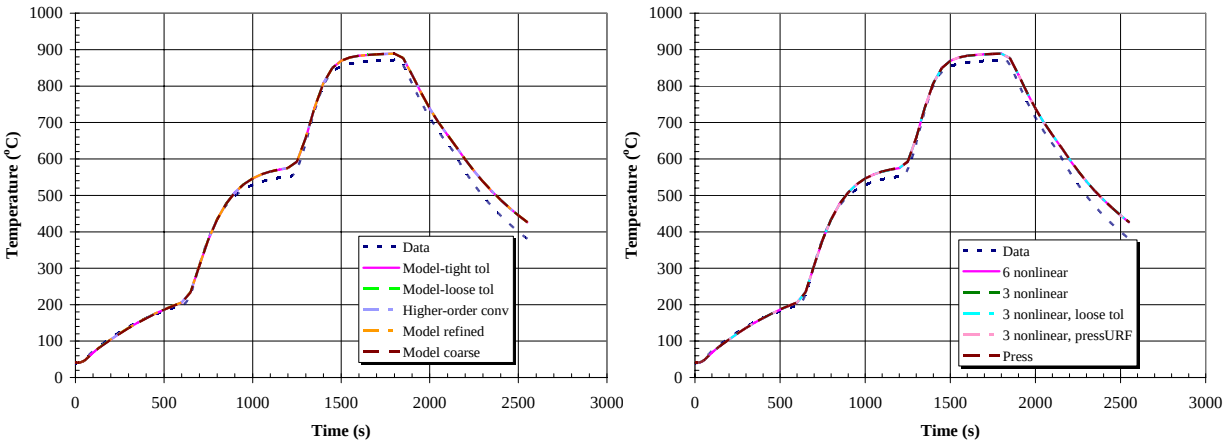

(j) TC34

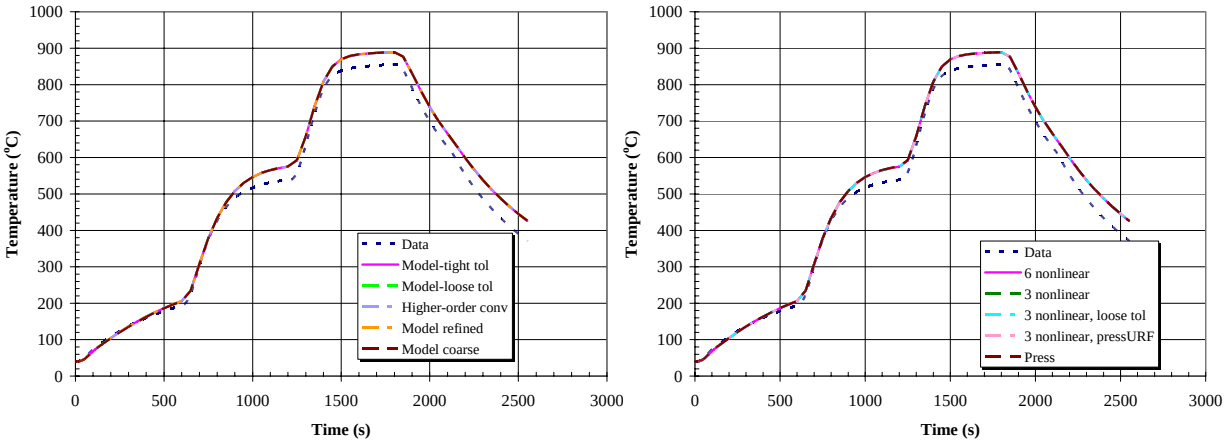

(k) TC35

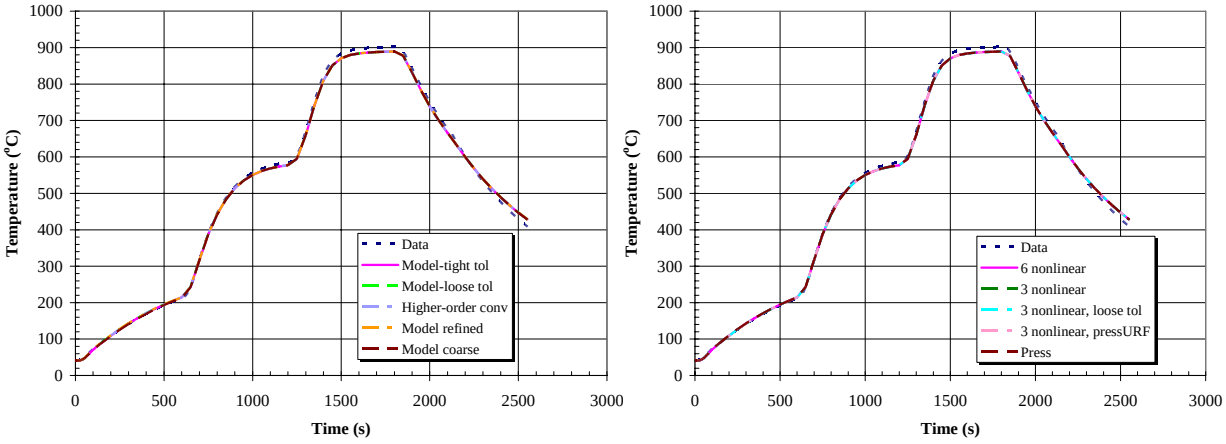

(l) TC36

Figure 16. Laminar Flow Results Comparison to Measure Data, (j) TC34, (k) TC35, and (l) TC36.

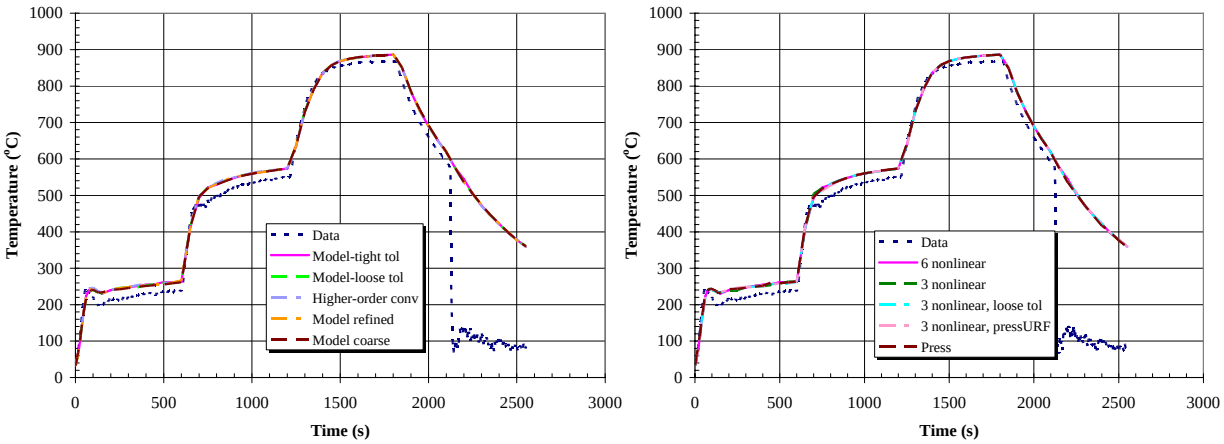

(a) TG1

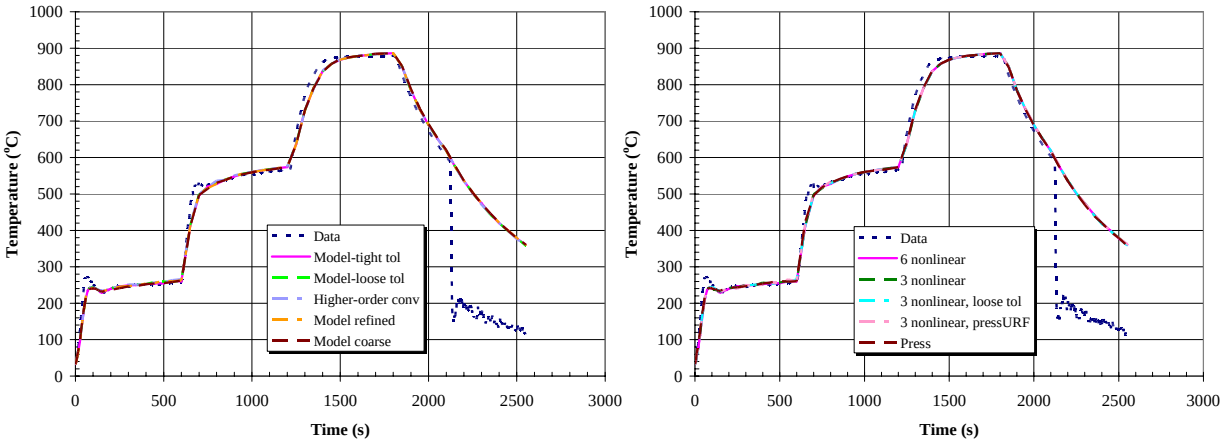

(b) TG3

Figure 17. Laminar Flow Results Comparison to Measure Data, (a) TG1, and (b) TG3.

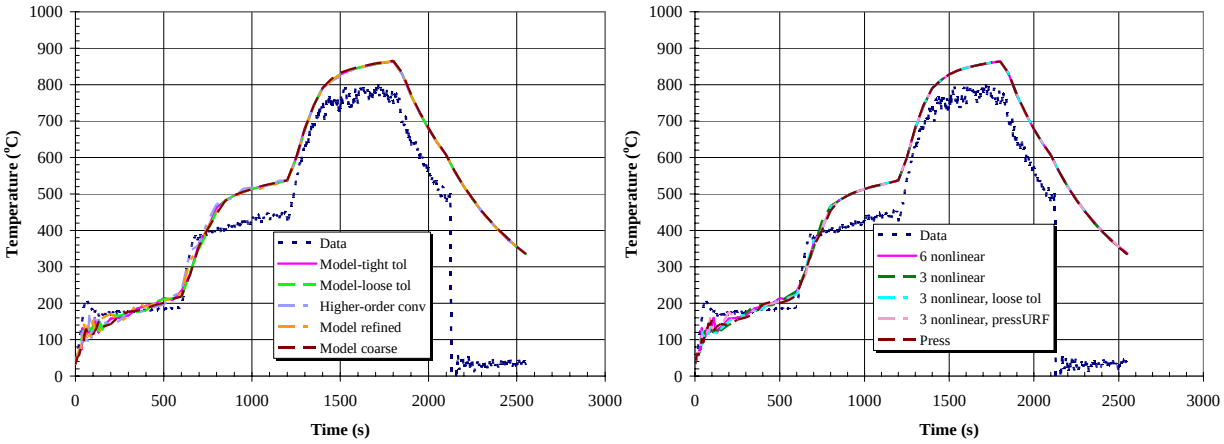

(c) TG2

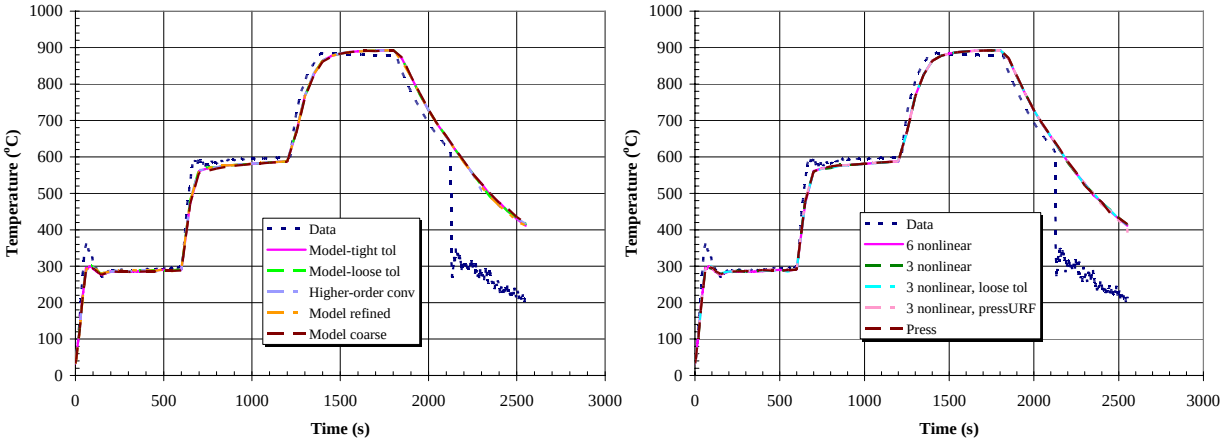

(d) TG4

Figure 18. Laminar Flow Results Comparison to Measure Data, (c) TG2, and (d) TG4.

For the most part, the coupled model temperature predictions compare very well to the measured temperature data in both the solid and fluid regions. The largest discrepancies between model and data in the solids region tend to occur at or near the top and bottom of the annulus, corresponding to TC locations 29 (top), 13 (bottom), 33 (near top), and 35 (near bottom). The best comparison between model and measured data in the solids region occurs at location TC25. The standard error and mean difference are 3.59 and 2.36°C, respectively. The worst comparison between model and measured data in the solids region occurs at location TC35. The standard error and mean difference are 20.41 and 12.30°C, respectively. The largest discrepancies between model and data in the fluid region tend to occur at the top and bottom of the annulus, corresponding to TG locations 4 (top), and 2 (bottom). TG2 located at the bottom of the annulus indicates the largest differences between predictions and

measurements. The best comparison between model and measured data in the fluid region occurs at location TG3. The standard error and mean difference are 22.67 and -9.48°C, respectively. The worst comparison between model and measured data in the fluid region occurs at location TG2. The standard error and mean difference are 65.89 and 21.19°C, respectively. Consistently, the coupled model under-predicts the temperature at or near the top of the annulus and it over-predicts the temperature at or near the bottom of the annulus. It is the top and bottom locations where the flow turns towards the other cylinder. It may be that the laminar flow model is not adequately capturing the flow field at these locations of importance from a fluid regimes perspective. That is, heat transfer either to or from the top and bottom locations is inadequate because of the laminar flow-only assumption. It is suspected that turbulent flow conditions may be in part the cause of this behavior. This is the topic of the next section in this report.

The assumption of a spatially uniform, constant temperature shroud boundary condition is not expected to change the preceding temperature predictions by all that much. If a more realistic spatially non-uniform shroud was modeled, the edge like TC predicted temperatures may all decrease slightly because of the influence of the edge of the shroud, but by how much is uncertain because the center of the shroud would also be slightly increased (see Figure 7), at least partially compensating for the decreases at the shroud edge. A similar, but reverse, scenario holds true of the center TCs. Because all of the test section TCs are actually located more towards the center of the shroud than at its edges, the average uniform shroud temperature is probably mostly representative.

With respect to the variations in the coupled model described in Table 2, it is noted from Figure 13 through Figure 18 that the laminar flow results are essentially identical for each of the cases considered. This is an important numerical assessment as simulation #1 required over 160 hours of wall-clock time while simulation #8 required only 30 hours, both providing essentially identical temperature results. Additionally, including compressibility effects in the energy equation being solved by Fuego did not influence the coupled model temperature predictions in either the fluid or solid regions; therefore, compressibility effects can be neglected. (The wall-clock times with or without compressibility effects were nearly the same, 81 versus 82 hours; however, it is noted that different linear solvers were used for simulations #2 and #9. Neglecting compressibility only slightly simplifies the Fuego portion of the input deck.) Finally, the comparison results also indicate that the working computational mesh does indeed provide a mesh independent solution (for the model parameters and flow conditions being compared).

Turbulent Flow Simulations

A number of different turbulent flow simulations are performed using the coupled model shown in Figure 5. Based on the results of the previous section, they include changes to residual tolerances required for the linear equation solves on continuity and all other scalars (e.g., Y-momentum), changes in the number of non-linear iterations, changes in pressure-correction equation under-relaxation factor (URF), different equation solvers, and different time filters applied to the turbulence equations solved in the $\overline{v^2}$-f turbulence model.

All of the $\overline{v^2}$-f turbulent flow simulations were executed using 128 processors on the *Thunderbird* Linux Cluster. It is noted that *none* of the turbulent flow simulations completed the requested amount of mother-nature time because of long runtimes dictated by time step limitations required by the time filtered turbulence equations.

The coupled model details for the working turbulent flow simulation (simulation #1 listed in Table 11) are given below in Table 12. This simulation and all others listed in Table 11 uses fourth-order smoothing with timestep scaling as the pressure projection method. The governing conservation equations are solved one-by-one (segregated solver). Simulation #2 uses the model inputs as described in Table 13. Note that the changes from the working case coupled model are highlighted in Table 13 in red. The second simulation serves solely to increase the speed of the coupled simulations by reducing the stringency on the linear equation solves and the total number of non-linear iterations. Additionally, the URF for the pressure-correction equation has also been reduced.

Table 11. $\overline{v^2}$-*f* Turbulent Flow Simulation Descriptions.

#	Legend Entry	Description	Clock (hrs)	Details in
1	Model-Turb	Working turbulent flow simulation	960*	Table 12
2	3 nonlin, loose tol, pressURF	Reduced stringency on residual tolerances required for the linear solve on continuity and other scalars, Reduced number of non-linear iterations, Changes to pressure correction URF	96*	Table 13
3	Alt solver	Alternative equation solution method, Reduced stringency on residual tolerances required for the linear solve on continuity and other scalars, Reduced number of non-linear iterations, Changes to pressure correction URF	96*	Table 13, Table 14
4	Increased time filter	Increased time filter, Reduced stringency on residual tolerances required for the linear solve on continuity and other scalars, Reduced number of non-linear iterations, Changes to pressure correction URF	96*	Table 13, Table 15

* - Simulation not completed

Table 12. Problem Setup Details for Turbulent Flow Simulation #1.

Model Input	Setting
Fuego continuity solution method	Aztec GMRES
Fuego continuity preconditioning method	DD-ILUT
Residual norm tolerance continuity	10^{-6}
Residual norm tolerance Helmholtz Function	10^{-7}
Fuego scalar solution method	Aztec GMRES
Fuego scalar preconditioning method	SYMMETRIC-GAUSS-SEIDEL
Residual norm tolerance scalars	10^{-4}
Residual norm tolerance turbulence dissipation	10^{-5}
Calore temperature solution method	Aztec CG
Calore preconditioning method	DD-ICC
Residual norm tolerance	10^{-8}
Turbulence time filter	0.01 seconds
Turbulence model Prandtl number (constant)	0.9
Upwind method	MUSCL
First order upwind factor	0.5
Fuego non-linear iterations	6
Calore non-linear iterations	5
URF pressure, momentum	0.8, 0.8
URF turbulence quantities all	0.6
Number of hexahedral elements	612,000

Table 13. Problem Setup Details for Turbulent Flow Simulation #2.

Model Input	Setting
Fuego continuity solution method	Aztec GMRES
Fuego continuity preconditioning method	DD-ILUT
Residual norm tolerance continuity	10^{-2}
Residual norm tolerance Helmholtz Function	10^{-3}
Fuego scalar solution method	Aztec GMRES
Fuego scalar preconditioning method	SYMMETRIC-GAUSS-SEIDEL
Residual norm tolerance scalars	10^{-2}
Residual norm tolerance turbulence dissipation	10^{-3}
Calore temperature solution method	Aztec CG
Calore preconditioning method	DD-ICC
Residual norm tolerance	10^{-6}
Turbulence time filter	0.01 seconds
Turbulence model Prandtl number (constant)	0.9
Upwind method	MUSCL
First order upwind factor	0.5
Fuego non-linear iterations	3
Calore non-linear iterations	5
URF pressure, momentum	0.3, 0.8
URF turbulence quantities all	0.6
Number of hexahedral elements	612,000

Simulation #3 uses a different solution and preconditioning method for the pressure solve associated with the fluids equations as indicated in Table 14, all other model settings are the same as those given in Table 13.

Table 14. Changes made to Turbulent Flow Simulation #3.

Model Input	Setting
Fuego continuity solution method	Aztec BICGSTAB
Fuego continuity preconditioning method	JACOBI*

* - the DD-ILUT preconditioning method diverged immediately

Simulation #4 increases the time filter slightly as indicated in Table 15; all other model settings are the same as those given in Table 13.

Table 15. Change made to Turbulent Flow Simulation #4.

Model Input	Setting
Turbulence time filter	0.025 seconds

During the course of performing the turbulent flow simulations using the $\overline{v^2}$-f turbulence model (see Reference 1 and Reference 6 for details regarding the use of this particular turbulence model, in general, and for its use in low-level turbulent natural convection), it was found that the default time filter of k/ε, also known as the eddy rollover time, resulted in terrible instabilities in the turbulence equations as the source terms in both the k-equation and the hyperbolic (Helmholtz Function) f-equation became increasing too large and the solution of the governing equations very rapidly diverged. Ultimately, only about 7 seconds of mother-nature time was simulated under these limiting conditions. Consequently, a narrower filter width time filtering approach[7] is also considered in this analysis.

The implication of a filter, either spatial or temporal, applied to the governing equations is that it separates the responsibility of capturing the inherent dynamics of the flow field into the discretized partial differential equations and into the subfilter engineering turbulence model. As the time filter width is decreased, more of the dynamics is captured directly by the discretized partial differential equations and less is required to be modeled. In this instance, the

[7] Sheldon R. Tieszen, Stefan P. Domino, and Amalia R. Black, "Validation of a Simple Turbulence Model Suitable for Closure of Temporally-Filtered Navier-Stokes Equations Using a Helium Plume," SAND2005-3210, June 2005.

(narrowing) time filtering approach in effect controls the turbulence production terms associated with the subfilter engineering model as these terms are multiplied directly by the time filter, which is smaller than the eddy rollover time.

This turbulence model is referred to as the temporally filtered Navier-Stokes (TFNS) equations (refer to Reference 7 for a more detailed description). It represents a compromise between long-duration time filtering (using the eddy rollover time) of a Reynolds Averaged Navier-Stokes (RANS) approach and the necessarily small spatial filters associated with the Large Eddy Simulation (LES). The narrow time filter is also associated with the turbulent viscosity as described by equation (15) in Reference 7. The turbulent viscosity is multiplied by the narrower time filter, instead of the eddy rollover time, to ensure that the affects of resolved (on the mesh) and modeled turbulence production are properly accounted for in the mean flow equations. (Note that a turbulence model does not explicitly simulate the details of the turbulent motion itself; but only the *effect* that turbulence has on the mean flow behavior.) Therefore, use of the typical eddy rollover time in the turbulent viscosity definition assumes that all of the turbulence production is modeled, which is not the case in this analysis. It is assumed that some of the turbulence production is resolved on the grid itself so the turbulent viscosity is adjusted accordingly.

A key advantage of the TFNS formulation is its applicability in the near-wall region. The viscosity affected region near a wall contains sufficiently high enough frequency turbulence that it should naturally be captured in the engineering model ($\overline{v^2}$-f) applied in this analysis. That is, high frequency turbulence fluctuations are naturally filtered out of the mean flow equations except through the modeled terms. To ensure that this is the case, it is necessary to consider a larger time filter (so that more effects are naturally modeled) than the one applied in Table 12, in the event that the selected grid size is too large (probably the case) to resolve the turbulence in the boundary layer. If the time filter is too small and the grid is too coarse, then this influence from turbulence will go un-captured. If, however, the time filter is larger, the influence of the turbulence will at least be captured in the mean flow equations by the subfilter engineering model (in this case by $\overline{v^2}$-f).

Time Step Requirements

Unlike in the laminar flow cases described in the previous section, the TFNS formulation dictates somewhat stringent time step requirements. Although the analyst still endeavored to achieve as large a time step as possible, the TFNS formulation called for a time step size on the order of less than half the temporal filter width (one forth would be preferable). A CFL limit of 1.0 is

specified for the turbulent flow simulations performed for this report. Unfortunately, this resulted in time step sizes slightly greater than half the time filter width of 0.01 seconds (simulations #1, 2, and 3). In a personal communication with S. Tieszen[8], this occurrence was described as a violation of the Nyquist criteria, which requires at least two points within the cutoff filter width. In an effort to better achieve this TFNS based restriction, a CFL limit of 1.0 is maintained while the time filter width is increased from 0.01 to 0.025 seconds. The initial simulation time step is 0.0005 seconds with a time step change factor of 1.2.

Comparison of Turbulent Flow Results to Measured Temperature Data

Each of the four simulations described in Table 11 are plotted in the following figures. The legends in each of the following figures correspond to the entry given in the second column in Table 11. Note also that the working laminar flow result is also included for convenience. Thermocouple (TC) locations 1, 5, 9, 13, 17, 21, 25, 29, 33, 34, 35, and 36 are illustrated from the solids region, and, gas temperature (TG) locations 1, 2, 3, and 4 are illustrated from the fluid region. The coupled model results shown in this section are all based on the approximation of the experimental heating schedule as shown in Figure 7. Figure 19 through Figure 24 illustrate the coupled model temperature predictions, with comparison to measured data, in the solids region at these TC locations. Figure 25 and Figure 26 illustrate the coupled model temperature predictions, with comparison to measured data, in the fluid region at these TG locations. It is noted that the gas temperature measurements are corrected for thermal radiation effects as described in Reference 3 in section 2.1.2.2 of that document. Subsequently, the comparison made at the four TG locations in this report is for a fluid temperature measurement without a thermal radiation contribution.

In each of the following figures presented for the turbulent flow cases, it is noted that all of the predicted temperature curves essentially *overlay* one another. This is indeed the desired result as the coupled flow simulations developed for this analysis and listed in Table 11 are performed to either increase the efficiency of a computation (by reducing the wall clock time) or to assess the appropriateness of an assumption applied to the model.

[8] Personal Communication with Sheldon R. Tieszen, Email dated on Friday, August 11, 2006.

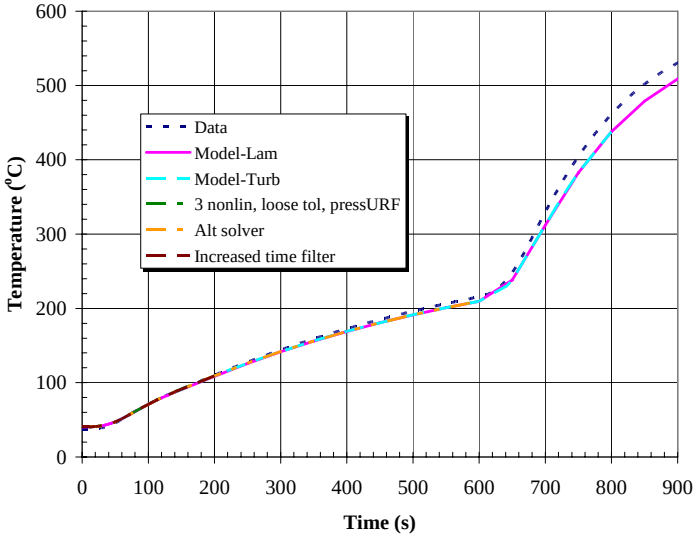

(a) TC1

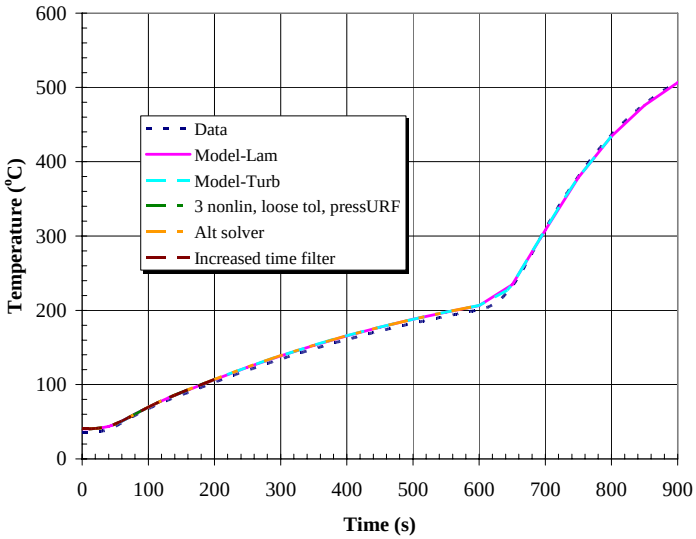

(b) TC5

Figure 19. Turbulent Flow Results Comparison to Measure Data, (a) TC1 and (b) TC5.

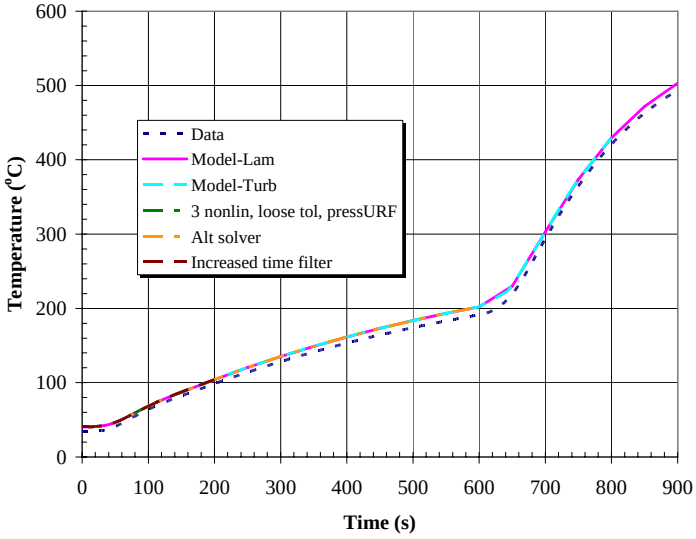

(c) TC9

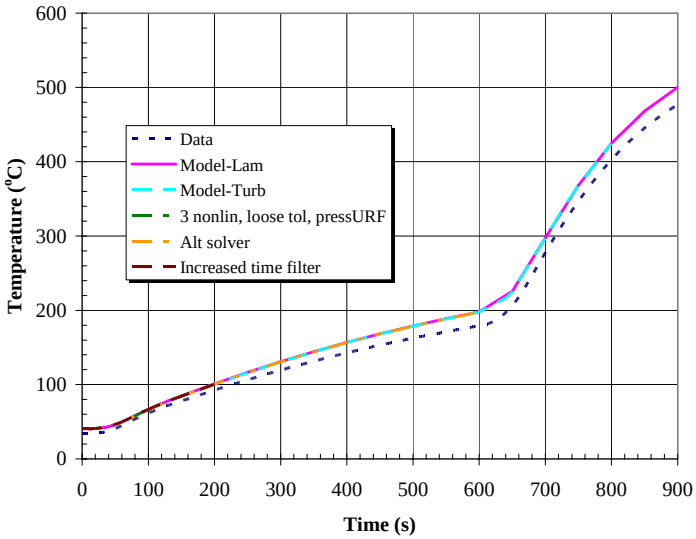

(d) TC13

Figure 20. Turbulent Flow Results Comparison to Measure Data, (c) TC9 and (d) TC13.

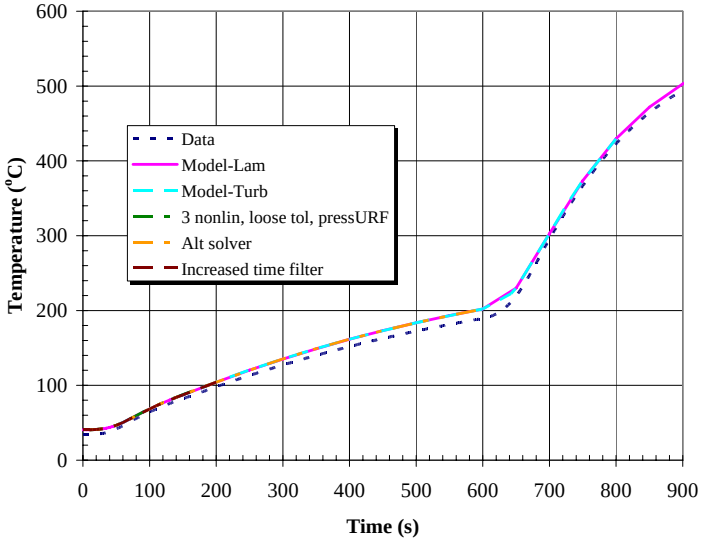

(e) TC17

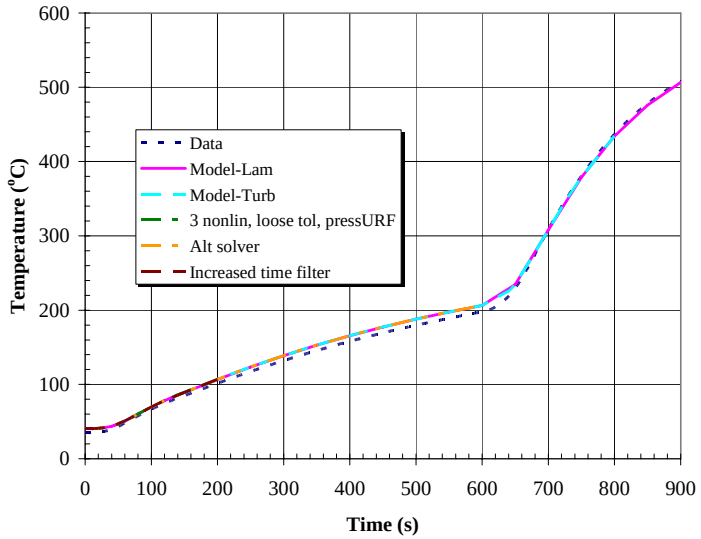

(f) TC21

Figure 21. Turbulent Flow Results Comparison to Measure Data, (e) TC17 and (f) TC21.

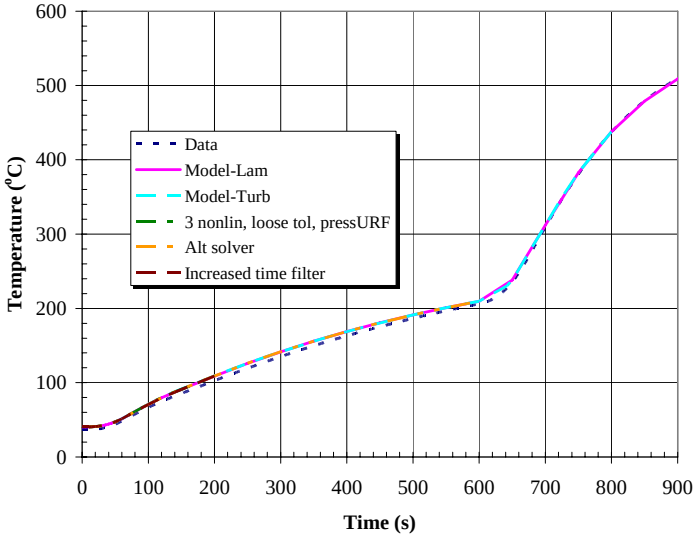

(g) TC25

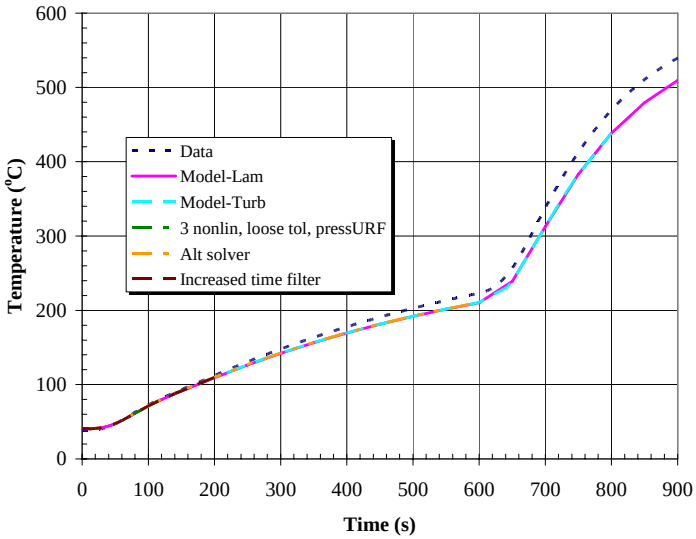

(h) TC29

Figure 22. Turbulent Flow Results Comparison to Measure Data, (g) TC25 and (h) TC29.

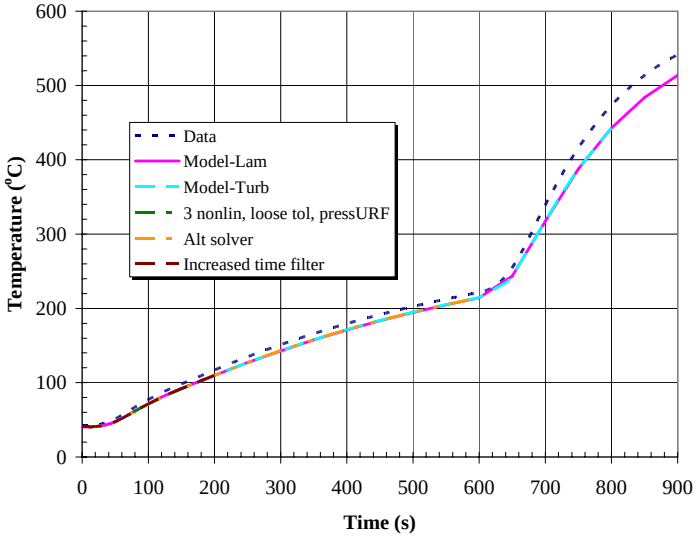

(i) TC33

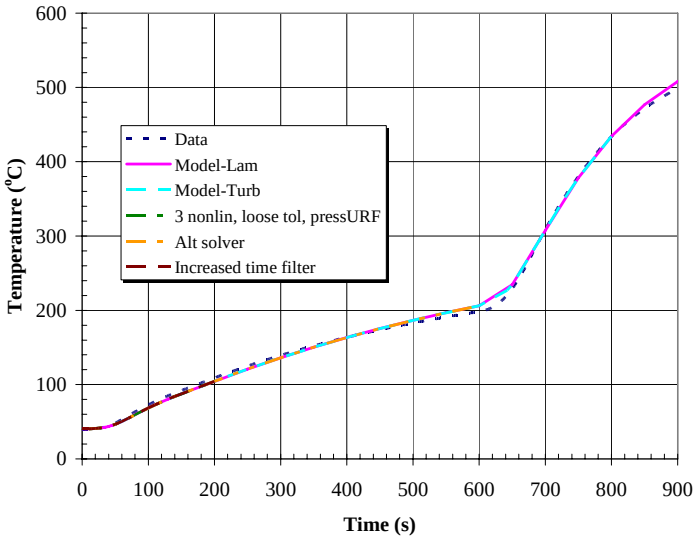

(j) TC34

Figure 23. Turbulent Flow Results Comparison to Measure Data, (i) TC33 and (j) TC34.

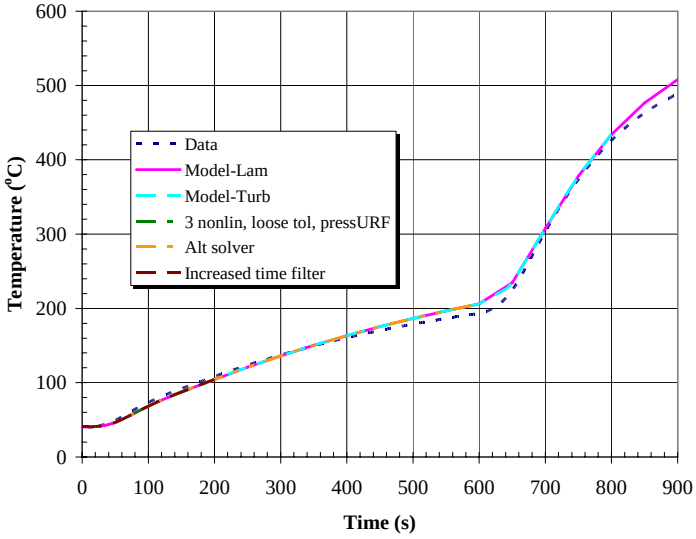

(k) TC35

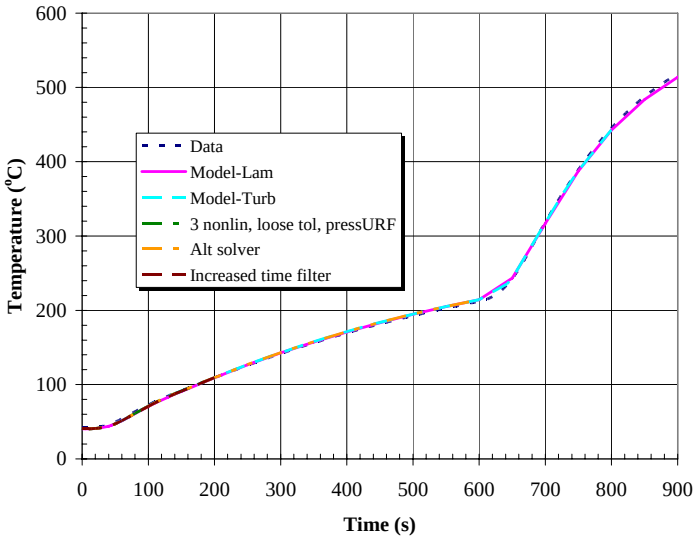

(l) TC36

Figure 24. Turbulent Flow Results Comparison to Measure Data, (k) TC35 and (l) TC36.

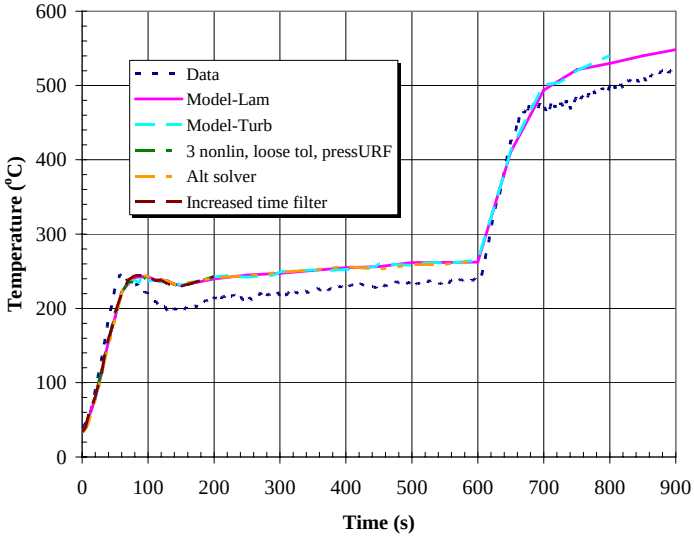

(a) TG1

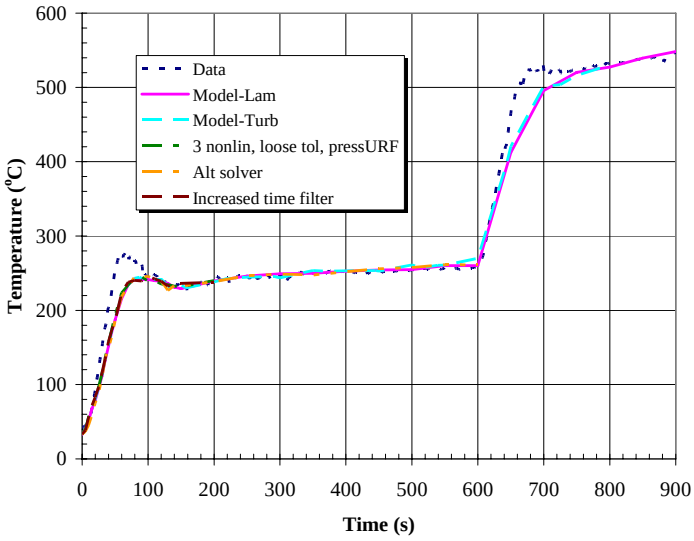

(b) TG3

Figure 25. Turbulent Flow Results Comparison to Measure Data, (a) TG1 and (b) TG3.

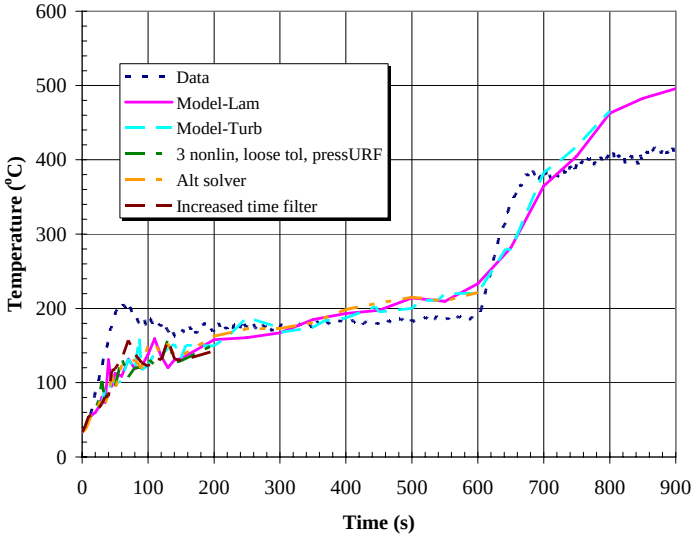

(c) TG2

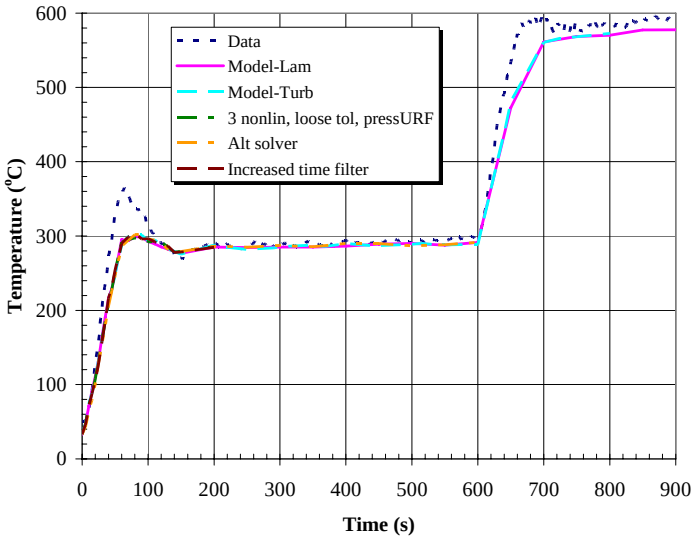

(d) TG4

Figure 26. Turbulent Flow Results Comparison to Measure Data, (c) TG2 and (d) TG4.

Like the previous section, the coupled model turbulent flow temperature predictions compare very well to the measured temperature data in both the solid and fluid regions. Additionally, the turbulent flow model predictions are nearly identical to the laminar flow results. This is, for the most part, expected based on anticipated flow conditions within the fluid domain. The primary differences are expected to occur at the top and bottom of the annulus, where the flow turns and conditions are such that transition to (low-level) turbulence is a possibility based on the results of previous work in the heat transfer literature (refer to Reference 4). The primary differences between laminar and turbulent predictions do in fact occur at the bottom of the annulus. This is also where the largest departure from the measured data occurs.

The differences between each of the turbulent flow cases described in Table 11 are indeed interesting. Although the predicted temperature trends are identical between cases, the resulting amount of mother-nature time is different. It is noted that each additional turbulent flow simulation was allowed only 96 hours of total wall clock time. Simulated times were 227, 625, and 246 seconds for simulations #2, #3, and #4, respectively. For comparison purposes, simulation #1 reached a time of only 88 seconds after 96 hours of wall clock time. The outlier here is of course *simulation #3*. Recall from Table 14 that only the linear equation solution and preconditioning methods applied to the pressure solve are changed (when compared to simulation #2), with, quite frankly, an extraordinary amount of additional mother-nature time simulated. From the figures, it is evident that its results are the same as the other turbulent flow cases considered. However, *severe* instability with this solution method occurred in conjunction with the start of the second major transient shown in Figure 7. (When referring to Figure 7, be sure to subtract 480 seconds from the time axis as the initial constant temperature period performed during the test is not modeled.) At the start of the second transient, the turbulence equation's linear residuals dramatically increased and the entire Fuego equation solution set very rapidly diverged. It is clear, however, that the performance of this solution and preconditioning method warrants further consideration. It may be possible to selectively choose certain equation solver methods, based on expected flow conditions, and with the use of restarts achieve much longer simulation times for turbulent flows.

Simulation #4 uses an increased (from 0.01 seconds to 0.025 seconds) time filter required in the TFNS formulation. This change is meant to better satisfy both the time step requirement when using TFNS and to determine if the amount of damping represented in the mean flow equations is currently being under-represented when using such a small time filter (0.01 s). Two of the preceding figures are compressed in time and temperature to better view the early time temperature trends as shown in Figure 27.

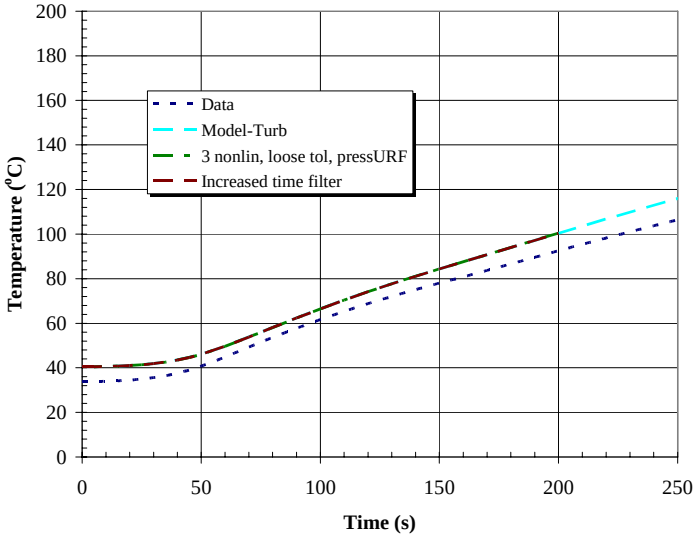

(a) TC13

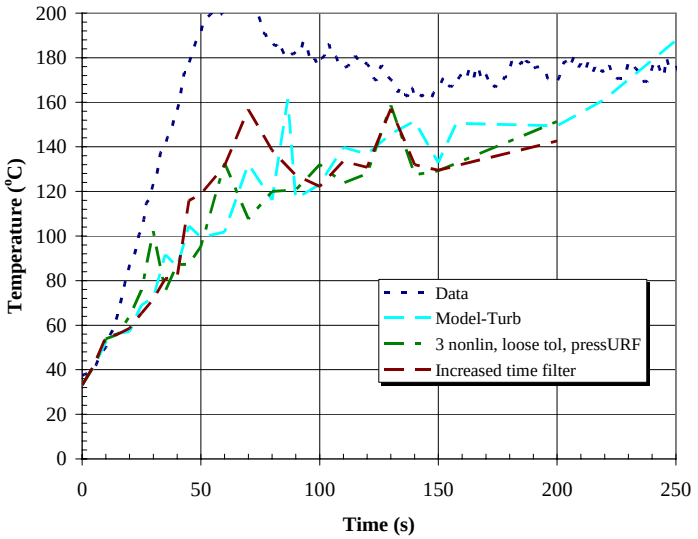

(b) TG2

Figure 27. Detailed Early Time Look at (a) TC13, and (b) TG2.

The plot of instantaneous temperature, in particular within the fluid region, makes it a little difficult to discern if the larger time filter makes a large difference, but it does appear overall that it is a somewhat better match when compared to the measured data. A still larger time filter may improve the predicted temperature response in the fluid during the early time periods, when the Rayleigh number is highest, but as previously commented, a value

probably less than the eddy rollover time will result in destabilizing the turbulence equations.

One final comment is made regarding the turbulent heat flux representation applied to the turbulent flow equations described in this report in Table 11. In each of the cases considered, the turbulent Prandtl number is assumed a constant value of 0.9. This assumption is typically reasonable for most turbulent flows with heat transfer except in those in which anisotropies are potentially important. This is indeed typically the case for low-level turbulent natural convection. This fact may explain some of the discrepancies noted in the comparisons to measured temperature data. Subsequently, it may be useful to consider turbulent heat flux representations like those described in a previous Sandia Internal Memorandum[9].

Summary

Fully coupled model predictions were compared to experimental temperature measurements made both in the solid regions (Calore Region) and the fluid region (Fuego Region). Turbulent and laminar flow temperature predictions were nearly identical for both regions. Predicted temperatures in the solid regions compared well to measured data. The largest discrepancies occurred at the bottom of the enclosed annulus. Predicted temperatures in the fluid region, for the most part, compared well to measured data. As before, the largest discrepancies occurred at the bottom of the annulus where the flow transitions to or is a low-level turbulent flow during the early heating period when estimated Rayleigh numbers were highest. The best comparison between model and measured data in the solids region occurred at location TC25. The standard error and mean difference were 3.59 and 2.36ºC, respectively. The worst comparison between model and measured data in the solids region occurred at location TC35. The standard error and mean difference were 20.41 and 12.30ºC, respectively. The best comparison between model and measured data in the fluid region occurred at location TG3. The standard error and mean difference were 22.67 and -9.48ºC, respectively. The worst comparison between model and measured data in the fluid region occurred at location TG2. The standard error and mean difference were 65.89 and 21.19ºC, respectively. Overall, the predicted temperatures compared well to measured temperature data from the March 22, 2006, Penlight experiment conducted at the thermal test complex at Sandia National Laboratories.

---

[9] Nicholas D. Francis, Jr., to Distribution, "Enhanced Flux Models Useful in Solving Low-Level Turbulent Natural Convection, Sandia Internal Memorandum, September 21, 2005.

A number of different *laminar* flow simulations were compared to each other and to the measured data. Nine cases were considered in all as described in Table 2. The predicted temperature results from each of the cases were essentially identical. This was an important finding because the working case coupled simulation required 160 hours of wall clock time whereas one of the less rigorous (with respect to solver settings, non-linear iterations, etc.) simulations required only 30 hours, a reduction in the computational requirement by a factor of over 5. Additionally, other model simplifications such as neglecting fluid compressibility effects were shown to have almost no impact on the model predictions that were compared to measured data. Finally, it was found that the working computational mesh was indeed grid independent (for the variables of interest).

A number of different *Turbulent* flow simulations were compared to each other, to laminar flow results, and to measured data. Four cases were considered in all as described in Table 11. Like in the laminar flow cases, the predicted temperature results from each of the turbulence cases were essentially identical to each other and to the working laminar flow case. Unlike the laminar flow cases, the turbulence model incurred an extremely heavy computational burden. A number of changes and modifications to the equation set solution parameters were identified in this report that greatly increased the speed of the turbulent flow computations, but the burden was still too large. Additionally, because mesh resolution cannot reasonably be refined to resolve enough of the dynamics of the flow field, recommendations regarding the use of a larger TFNS time filter to better model the influence turbulence has on the mean flow equations may be in order. Finally, other potentially more accurate representations used to estimate the turbulent heat flux for anisotropic thermally driven buoyant flows may improve turbulent flow predictions. However, it is likely that both of these recommendations would most likely degrade the overall efficiency of the turbulent flow computation.

References

[1.] SIERRA/Fuego Users Manual – 2.5, SAND2006-6084P, Sandia National Laboratories, June 4, 2007.

[2.] Calore; A Computational Heat Transfer Program. User Reference Manual version 4.4, Sandia National Laboratories, October 24, 2006.

[3.] Allen Ricks, Thomas Blanchat, and Dann Jernigan, "Validation Experiments to Determine Radiation Partitioning of Heat Flux to an Object in a Fully Turbulent Fire," SAND2006-3494, June 2006.

[4.] T. H. Kuehn, and R. J. Goldstein, "An Experimental Study of Natural Convection Heat Transfer in Concentric and Eccentric Horizontal Cylindrical Annuli." Journal of Heat Transfer, Transactions of the ASME, 100, 635-640. 1978.

[5.] K. Hanjalic', "One-Point Closure Models for Buoyancy-Driven Turbulent Flows," Annual Review of Fluid Mechanics, 34, pp. 321-347, 2002.

[6.] Nicholas D. Francis, Jr., "Characterization of Fuego for Laminar and Turbulent Natural Convection Heat Transfer," SAND2005-5085, August 2005.

[7.] Sheldon R. Tieszen, Stefan P. Domino, and Amalia R. Black, "Validation of a Simple Turbulence Model Suitable for Closure of Temporally-Filtered Navier-Stokes Equations Using a Helium Plume," SAND2005-3210, June 2005.

[8.] Personal Communication with Sheldon R. Tieszen, Email dated on Friday, August 11, 2006.

[9.] Nicholas D. Francis, Jr., to Distribution, "Enhanced Flux Models Useful in Solving Low-Level Turbulent Natural Convection, Sandia Internal Memorandum, September 21, 2005.

Distribution: Internal

1	MS-0382	01541	S. W. Bova
1	MS-0382	01541	S. P. Domino
1	MS-0382	01541	S. E. Gianoulakis
1	MS-0384	01540	H. S. Morgan
1	MS-0384	01500	A. C. Ratzel
1	MS-0735	06313	S. W. Webb
1	MS-0824	01510	M. R. Prairie
1	MS-0828	01544	A. R. Black
1	MS-0828	01544	K. J. Dowding
1	MS-0828	01544	A. A. Giunta
1	MS-0828	01544	V. J. Romero
1	MS-0836	01514	P. K. Notz
1	MS-0836	01516	D. Dobranich
1	MS-0836	01516	W. W. Erikson
5	MS-0836	01516	N. D. Francis
1	MS-0836	01516	E. S. Hertel
1	MS-0836	01516	M. L. Hobbs
1	MS-0836	01516	R. E. Hogan
1	MS-1135	01532	T. K. Blanchat
1	MS-1135	01532	A. L. Brown
1	MS-0836	01532	W. Gill
1	MS-1135	01532	A. J. Ricks
1	MS-1135	01532	S. R. Tieszen
1	MS-9014	08242	A. R. Ortega
1	MS-9409	08775	G. H. Evans
1	MS-9409	08775	C. D. Moen
1	MS-9409	08775	G. J. Wagner
2	MS-9018	08944	Central Technical Files
2	MS-0899	04536	Technical Library Files

Distribution: External

Darryl L. James, Ph. D.
Texas Tech University
Department of Mechanical Engineering
Box 41021
Lubbock, TX 79409-1021

Cuauhtemoc Aviles-Ramos, Ph.D.
ESA-Weapons Response Group MS P946
Los Alamos National Laboratory
P.O. Box 1663
Los Alamos NM, 87545